Unveiling energy pathways in AGN accretion flows with the warm corona model for the soft excess

D.R Ballantyne, V Sudhakar, D Fairfax, S Bianchi, B Czerny, A de Rosa, B de Marco, R Middei, B Palit, P. -O Petrucci, et al.

Monthly Notices of the ROYAL ASTRONOMICAL SOCIETY

MNRAS **530,** 1603–1623 (2024) https://doi.org/10.1093/mnras/stae944
Advance Access publication 2024 April 4

Unveiling energy pathways in AGN accretion flows with the warm corona model for the soft excess

D. R. Ballantyne [1]★ V. Sudhakar,[1] D. Fairfax,[1,2,3] S. Bianchi [4] B. Czerny,[5] A. De Rosa [6] B. De Marco,[7] R. Middei [8,9] B. Palit,[10] P.-O. Petrucci,[11] A. Różańska[10] and F. Ursini[4]

[1]*Center for Relativistic Astrophysics, School of Physics, Georgia Institute of Technology, 837 State Street, Atlanta, GA 30332-0430, USA*
[2]*Department of Physics, Morehouse College, 830 Westview Dr SW, Atlanta, GA 30314, USA*
[3]*Department of Aerospace Engineering, University of Michigan, 1320 Beal Avenue, Ann Arbor, MI 48109, USA*
[4]*Dipartimento di Matematica e Fisica, Università degli Studi Roma Tre, Via della Vasca Navale 84, I-00146 Roma, Italy*
[5]*Center for Theoretical Physics, Polish Academy of Sciences, Al. Lotnikov 32/46, PL-02-668 Warsaw, Poland*
[6]*INAF – Istituto di Astrofisica e Planetologie Spaziali, Via del Fosso del Cavaliere 100, I-00133 Roma, Italy*
[7]*Departament de Fìsica, EEBE, Universitat Politècnica de Catalunya, Av. Eduard Maristany 16, E-08019 Barcelona, Spain*
[8]*INAF – Osservatorio Astronomico di Roma, Via Frascati 33, I-00040 Monte Porzio Catone, Italy*
[9]*Space Science Data Center, SSDC, ASI, Via del Politecnico snc, I-00133 Roma, Italy*
[10]*Nicolaus Copernicus Astronomical Center, Polish Academy of Sciences, Bartycka 18, PL-00-716 Warszawa, Poland*
[11]*Univ. Grenoble Alpes, CNRS, IPAG, F-38000 Grenoble, France*

Accepted 2024 April 3. Received 2024 March 13; in original form 2024 January 15

ABSTRACT

The soft excess in active galactic nuclei (AGNs) may arise through a combination of relativistic reflection and the effects of a warm corona at the surface of the accretion disc. Detailed examination of the soft excess can therefore constrain models of the transport and dissipation of accretion energy. Here, we analyse 34 *XMM–Newton* observations from 14 type 1 AGNs with the REXCOR spectral model that self-consistently combines emission from a warm corona with relativistic reflection assuming a lamppost corona. The model divides accretion energy between the disc, the warm corona, and the lamppost. The *XMM–Newton* observations span a factor of 188 in Eddington ratio ($\lambda_{\rm obs}$) and 350 in black hole mass, and we find that a warm corona is a significant contributor to the soft excess for 13 of the 14 AGNs with a mean warm corona heating fraction of 0.51. The REXCOR fits reveal that the fraction of accretion energy dissipated in the lamppost is anticorrelated with $\lambda_{\rm obs}$. In contrast, the relationship between $\lambda_{\rm obs}$ and both the optical depth and the heating fraction of the warm corona appears to transition from an anticorrelation to a correlation at $\lambda_{\rm obs,t} \approx 0.15$. Therefore, at least one other physical process in addition to the accretion rate is needed to explain the evolution of the warm corona. Overall, we find that a warm corona appears to be a crucial depository of accretion energy in AGNs across a broad range of $\lambda_{\rm obs}$ and black hole mass.

Key words: accretion, accretion discs – galaxies: active – galaxies: Seyfert – X-rays: galaxies.

1 INTRODUCTION

Active galactic nuclei (AGNs) generate their luminosity from the release of gravitational potential energy as matter moves radially through an accretion disc. If the accretion flow is radiatively efficient, then the released energy is locally converted into photons and the disc shines brightly over a wide range of wavelengths, with the peak luminosity occurring in the ultraviolet (UV) for most AGNs (e.g. Pringle 1981; Frank, King & Raine 2002; Shakura & Sunyaev 2009). In addition to the optically thick thermal emission from the disc, AGNs are also strong X-ray emitters with, on average, $\lesssim$20 per cent of their bolometric luminosity released as a power law at photon energies $\gtrsim$1 keV before rolling over at energies $\gtrsim$100 keV (e.g. Mushotzky, Done & Pounds 1993; Vasudevan & Fabian 2007, 2009; Ricci et al. 2017; Duras et al. 2020). This X-ray power law is well described as originating in an optically thin Comptonizing corona of hot electrons situated close to the disc and central black hole (e.g. Galeev, Rosner & Vaiana 1979; Haardt & Maraschi 1991, 1993; Petrucci et al. 2001; Fabian et al. 2015, 2017; Kara et al. 2016; Alston et al. 2020). While the details of how and why accretion energy flows from the disc into the corona are not fully understood, it appears that magnetic fields in the disc and corona play a crucial role (e.g. Merloni & Fabian 2001; Jiang et al. 2019; Gronkiewicz & Różańska 2020; Gronkiewicz et al. 2023; Scepi, Begelman & Dexter 2024).

The X-ray spectrum of AGNs contains more complexity than just a simple power law. Superimposed on the power law are spectral lines and high-energy curvature consistent with reprocessing of the power law in optically thick material lying out of the line of sight, a process generally referred to as X-ray reflection (e.g. Fabian & Ross 2010; García & Kallman 2010). Moreover, most AGNs show an excess of emission above the extrapolated power law at energies $\lesssim$2 keV (a 'soft excess'; e.g. Piconcelli et al. 2005; Winter et al. 2012; Ricci et al. 2017). The soft excess may arise from X-ray reflection (e.g. Crummy et al. 2006), but it is also possible that a warm corona located near

★ E-mail: david.ballantyne@physics.gatech.edu

the surface of the accretion disc can contribute all or part of the soft excess (e.g. Magdziarz et al. 1998; Czerny et al. 2003; Różańska et al. 2015; Kubota & Done 2018; Middei et al. 2018, 2019, 2020; Porquet et al. 2018; Ursini et al. 2018, 2020; Xu et al. 2021a). Similar to the hot corona that produces the X-ray power law, a warm corona would be heated by accretion processes and Comptonize the thermal emission from the bulk of the disc. However, the warm corona is optically thick (with $\tau \gtrsim 10$), and $\approx$100$\times$ cooler than the hot corona located near the disc (e.g. Petrucci et al. 2018). If it exists, the warm corona would be another location to which accretion energy liberated in the disc is transported and dissipated. Therefore, it is important to determine the properties of any warm coronae in AGNs in order to fully understand the flow of energy in an accretion disc.

As the surface of the accretion disc is irradiated by the X-ray power law, the warm corona properties, and the resulting emission spectrum from the disc, are determined by the combined influence of both internal heating in the warm corona and the photoionization effects of the external X-rays (Ballantyne 2020; Ballantyne & Xiang 2020; Petrucci et al. 2020). In particular, the fraction of accretion energy dissipated in the warm corona has a strong impact on the resulting AGN X-ray spectrum and could be constrained by fitting with an appropriate model. Recently, the REXCOR model was made publicly available by Xiang et al. (2022). This spectral model assumes an optically thick accretion disc that extends to the innermost stable circular orbit (ISCO) and combines the effects of a warm corona with ionized relativistic reflection to predict the X-ray spectrum from the inner region of an AGN accretion disc. By dividing the liberated accretion energy between the disc, a warm corona, and a lamppost hot corona,[1] REXCOR provides an opportunity to quantitatively measure the fraction of accretion energy dissipated in both the warm and hot coronae. In this paper, we apply the REXCOR model to a sample of 34 *XMM–Newton* observations of 14 type 1 AGNs that span a factor of 188 in Eddington ratio and two decades in black hole mass. By examining how the REXCOR parameters vary across this sample, we will be able to better understand the nature of the warm corona in AGNs and how accretion energy is distributed through the disc.

The next section provides a short review of the assumptions and parameters of the REXCOR model, and the properties of the *XMM–Newton* AGN sample are described in Section 3. The results of fitting REXCOR models to the AGN sample are presented in Section 4. The implications of our results on our understanding of the AGN soft excess and the warm corona model are discussed in Section 5. Finally, we summarize and draw conclusions in Section 6.

2 REVIEW OF THE REXCOR AGN SPECTRAL MODEL

The REXCOR model is fully described by Xiang et al. (2022) and so only a brief review of its features is presented here. A REXCOR spectrum is calculated from the inner 400 r_g (where $r_g = GM/c^2$ is the gravitational radius of a black hole with mass M) of an AGN accretion disc, illuminated by an X-ray power law from a hot corona placed at a height of h above the central black hole (i.e. a lamppost geometry; e.g. Matt, Perola & Piro 1991; Martocchia & Matt 1996; Dauser et al. 2013). The power law has a photon index Γ and has low- and high-energy cut-offs at 30 eV and 300 keV, respectively. The black hole has a spin a, and the fitting functions of Fukumura & Kazanas (2007) are used to account for how relativistic light bending affects the illumination of the disc. In addition to this external radiation from the hot corona, REXCOR also includes internal heating from a warm corona of Thomson thickness τ at the surface of the disc. This heated layer has a fixed density and interacts with the external X-rays and the thermal blackbody emission arising from the bulk of the disc.

In REXCOR the luminosity of the lamppost and the amount of heat released in the warm corona are fixed fractions of the accretion disc dissipation rate $D(r, \lambda)$, where r is the radius of the disc (in units of r_g) and λ is the Eddington ratio (Shakura & Sunyaev 2009). A fraction f_X of $D(r, \lambda)$ within $r = 10\,r_g$ powers the hot corona luminosity, while an energy flux $h_f D(r, \lambda)$ is uniformly distributed in the warm corona layer of the disc (with Thomson depth τ). Any remaining flux at a particular radius, $(1 - f_X - h_f)D(r, \lambda)$, is injected into the bottom of the warm corona zone as a blackbody.

A REXCOR model is computed by splitting the disc into multiple annuli and self-consistently calculating the emission from the disc surface from each annulus. The spectrum of each ring includes (i) the effects of ionized reflection due to illumination by the power-law continuum produced by the lamppost hot corona, (ii) the emission and scattering effects of the warm corona at the disc surface, and (iii) the thermal blackbody produced by the bulk of the disc. The effects of relativistic blurring (using the RELCONV_LP model with an inclination angle of 30°; Dauser et al. 2013) and the radial change in disc density are included for each annulus. Finally, the individual blurred reflection spectra are then integrated to produce a single spectrum that can be used to fit data between 0.2 and 100 keV.

As shown by Xiang et al. (2022), the parameters of the REXCOR models impact the resulting spectra in distinct ways. The warm corona heating fraction h_f and optical depth τ both strongly influence the size, shape, and smoothness of the soft excess. For a given h_f, a larger τ will reduce the soft excess strength and smoothness as the heat released in the warm corona is dissipated in a thicker layer of gas. Similarly, for a fixed τ, an increasing h_f will yield a hotter, more ionized warm corona that produces a stronger soft excess that extends to higher energies. Changes to the hot corona heating fraction f_X affect the REXCOR model by impacting the size of the soft excess relative to the power law, as well as influencing the ionization state of the reflection features in the spectrum (analogous to the ionization parameter ξ in standard reflection models; García & Kallman 2010). Finally, the photon index Γ changes the shape of the spectra at energies >2 keV where the impact of the power law is most important.

Xiang et al. (2022) released eight different REXCOR grids that differ in the assumed lamppost height (either 5 or 20 r_g), accretion rate (either $\lambda = 0.01$ or 0.1), and black hole spin (either $a = 0.9$ or 0.99). Each grid contains over 20 000 individual spectra, spanning a broad range of Γ, τ, f_X, and h_f. In this paper, we make use of new REXCOR grids[2] that increases the range of Γ (from $\Gamma =$ 1.7–2.2 to 1.5–2.2) with the other parameters unchanged from the original release ($0.02 \leq f_X \leq 0.2$; $0 \leq h_f \leq 0.8$; $10 \leq \tau \leq 30$). Therefore, fitting AGN X-ray spectra with REXCOR grids can test for the presence of a warm corona (i.e. if $h_f > 0$), and constrain how the accretion energy is divided between the lamppost and the disc surface. We note that since the REXCOR models assume the presence of an optically thick accretion disc down to the ISCO and a lamppost corona, then, by construction, f_X is not allowed to be 0, and REXCOR models always contain a contribution from relativistic ionized reflection.

[1] This differs from the Petrucci et al. (2020) model that divides energy between the disc and the warm corona.

[2] These expanded grids are now available through the XSPEC website.

Table 1. Details of the AGN sample including the *XMM–Newton* Observation ID, redshift, black hole mass (from Bianchi et al. 2009), and bolometric Eddington ratio (λ_{obs}; estimated by Petrucci et al. 2018). All sources are radio-quiet type 1 AGNs and have >150 000 counts in their 0.3–12 keV EPIC-pn spectra. Petrucci et al. (2018) provide details on the selection of the parent sample.

Object	Redshift	$\log(M_{BH}/M_{\odot})$	Obs ID	λ_{obs}
1H 0419−577	0.104	8.58	0604720301	0.156
			0604720401	0.128
ESO 198−G24	0.0455	8.48	0305370101	0.012
			0067190101	0.013
HE 1029−1401	0.0858	8.73	0203770101	0.102
IRASF 12397+3333	0.0435	6.66	0202180201	0.615
Mrk 279	0.0304	7.54	0302480401	0.127
			0302480501	0.12
			0302480601	0.121
Mrk 335	0.0257	7.15	0600540501	0.186
			0600540501	0.172
Mrk 509	0.0343	8.16	0601390201	0.127
			0601390301	0.123
			0601390401	0.157
			0601390501	0.176
			0601390601	0.197
			0601390701	0.157
			0601390801	0.146
			0601390901	0.131
			0601391001	0.135
			0601391101	0.134
Mrk 590	0.0263	7.68	0201020201	0.009
NGC 4593	0.00831	6.73	0109970101	0.053
			0059830101	0.075
PG 0804+761	0.1	8.24	0605110101	0.402
PG 1116+215	0.1765	8.53	0201940101	0.384
			0554380101	0.404
			0554380201	0.373
			0554380301	0.425
Q0056−363	0.1641	8.95	0205680101	0.053
RE 1034+396	0.0424	6.41	0675440301	1.691
UGC 3973	0.0221	7.72	0400070201	0.034
			0400070301	0.025
			0400070401	0.028

3 DESCRIPTION OF AGN SAMPLE AND SPECTRAL FITTING METHOD

REXCOR models are applied to a sample of *XMM–Newton* observations of bright, radio-quiet type 1 AGNs. Our sample is drawn from the one studied by Petrucci et al. (2018), which was selected to have good UV coverage with the Optical Monitor. The UV photometry is not used when fitting REXCOR models, so this criterion should not influence our results.

From this parent sample, we select only those observations with photon indices inside the REXCOR range and have >150 000 counts in their European Photon Imaging Camera (EPIC)-pn 0.3–12 keV spectra. Observations with total counts below this limit did not provide useful constraints on the key REXCOR parameters (e.g. h_f, f_X, and τ) despite acceptable fits. Three of the five observations of NGC 4593 that lie above our count limit (Obs IDs 0740920201, 0740920501, and 0740920601) also give poorly constrained REXCOR parameters (see also Xiang et al. 2022) and are removed from further analysis. Our final sample therefore contains 34 *XMM–Newton* observations of 14 AGNs and spans over two decades in both black hole mass and accretion rate. Table 1 provides the details of the sample, including the estimated bolometric Eddington ratio from each observation, λ_{obs}, as determined by Petrucci et al. (2018).

We analyse the same *XMM–Newton* spectra as Petrucci et al. (2018), and details of the data reduction are provided in that paper. For all sources, we fit the 0.3–12 keV EPIC-pn (Strüder et al. 2001) spectra, except for Mrk 509 that is fit only for energies >0.76 keV to avoid large features associated with the complex multicomponent warm absorber (Detmers et al. 2011; Petrucci et al. 2013; Kaastra et al. 2014). The spectral fits are performed with XSPEC v.12.13.0 (Arnaud 1996) using χ^2 statistics, and error bars are reported using a $\Delta\chi^2 = 2.71$ criterion. Each observation is fit with the following model (in XSPEC notation):

$$phabs \times WA \times (powerlaw + \text{REXCOR} + xillver),$$

where *phabs* is neutral Galactic absorption to the AGN (HI4PI Collaboration 2016), *WA* is a XSTAR-derived warm absorber grid (Walton et al. 2013) located at the redshift of the source, *powerlaw* is the primary X-ray continuum[3] with photon index Γ, and *xillver* is a neutral reflection spectrum (e.g. García & Kallman 2010) accounting for reprocessing from material far from the black hole. The photon index is linked across the *powerlaw*, *xillver*, and REXCOR models. The free parameters of the warm absorber grid are the column density and ionization parameter. The abundances of the *WA*, *xillver*, and REXCOR models are all fixed to solar. The inclination angle and cut-off energy of the *xillver* component are fixed at 30° and 300 keV, respectively, in order to match the assumptions of REXCOR. The *cflux* command is applied to the *powerlaw*, REXCOR, and *xillver* models to determine the 0.3–10 keV normalizations and fluxes of each component.

The REXCOR grids are separated by the Eddington ratio, with a set calculated for $\lambda = 0.01$ and one for $\lambda = 0.1$. In addition to the increase in luminosity, the higher value of λ corresponds to a lower disc density (Xiang et al. 2022), as predicted for radiation-pressure-dominated discs (e.g. Svensson & Zdziarski 1994). As a result, the $\lambda = 0.1$ grids predict a more highly ionized disc with weaker reflection features. Here, we use the $\lambda = 0.1$ grids for all observations with $\lambda_{obs} > 0.05$ and the $\lambda = 0.01$ grid otherwise (Appendix C shows that our results are robust to this choice). Two of the AGN observations are estimated to have $\lambda_{obs} = 0.053$ (Obs ID 0109970101 from NGC 4593 and the one from Q0056−363) and thus we try both sets of REXCOR grids when fitting this particular data set. We find that the $\lambda = 0.01$ grids give the lowest χ^2 for Q0056−363, while the $\lambda = 0.1$ grids yield the best fit for the NGC 4593 observation.

For a given λ, there are four REXCOR grids covering the two different values of lamppost height ($h = 5$ or $20\,r_g$) and black hole spin ($a = 0.9$ or 0.99). All four grids are used when fitting the first observation of an AGN with the results recorded for the grid yielding the lowest χ^2. Once the best fit is determined, the same value of a is used for any subsequent observation of that AGN,[4] but both values of h continue to be tested for all observations.

[3]As with standard reflection models, this *powerlaw* component is distinct from the one used in computing the REXCOR model by Xiang et al. (2022) and is included to account for the uncertainties in the actual disc/corona geometry in AGNs. The values of f_X measured by the spectral fits are determined by the shape and features of the REXCOR models, computed in the context of a lamppost corona (Xiang et al. 2022).

[4]By construction, all observations have comparably good statistics, so the value of a does not depend on which observation was fit first. The only exception is NGC 4593, where the second observation (Obs ID 0059830101) yielded a better constraint on a than the first observation.

Table 2. Summary of the correlation analysis performed on the REXCOR parameters and the observed Eddington ratio, λ_{obs}. The top part of the table gives Kendall's τ correlation coefficient and the corresponding p-value for the relationships with f_X (Fig. 1), Γ (Fig. 2), and the 0.3–10 keV flux ratio (Fig. 4). The lower part of the table provides the average p-values for different transition Eddington ratios ($\lambda_{obs,t}$) when testing if the τ–λ_{obs} and h_f–λ_{obs} relations (Fig. 3) change from a negative to positive correlation at $\lambda_{obs,t}$. The error bars on Kendall's τ and p-values are computed from sampling the uncertainties in each of the REXCOR parameters 10^4 times. The largest of the two plotted error bars (or the single error bar for pegged data) is used to define the symmetric Gaussian uncertainty for each point. All statistical calculations performed using PYMCCORRELATION (Isobe, Feigelson & Nelson 1986; Privon et al. 2020).

Relationship with λ_{obs}	Kendall's τ	p-value
f_X	$-0.57^{+0.06}_{-0.05}$	$1.6^{+16}_{-1.4} \times 10^{-6}$
Γ	0.26 ± 0.06	$0.031^{+0.063}_{-0.023}$
(0.3–10) keV flux ratio	0.55 ± 0.03	$3.2^{+7.5}_{-2.2} \times 10^{-6}$
(0.3–10) keV flux ratio (no RE 1034+396)	0.53 ± 0.03	$1.3^{+3}_{-0.9} \times 10^{-5}$
τ and h_f transition λ_{obs} (i.e. $\lambda_{obs,t}$)	Mean p-value	Mean p-value (no Mrk 335)
0.10	$0.10^{+0.24}_{-0.08}$	$0.088^{+0.216}_{-0.067}$
0.12	$0.046^{+0.135}_{-0.033}$	$0.049^{+0.111}_{-0.037}$
0.15	$0.0046^{+0.0149}_{-0.0034}$	$0.0050^{+0.0186}_{-0.0039}$
0.20	$0.095^{+0.103}_{-0.060}$	$0.12^{+0.086}_{-0.088}$

4 RESULTS

Tables of the results of the spectral fitting are found in Appendix A while Appendix B contains plots showing the best-fitting models and residuals. In this section, we analyse the best-fitting parameters from the REXCOR models and demonstrate how these change with the AGN Eddington ratio.[5] A discussion showing that our model assumptions do not impact the results in this section is found in Appendix C.

4.1 Basic properties of fits

Examination of the fit results in Table A1 shows that our assumed model provides a good description of the spectrum for all 34 observations. The median reduced χ^2 of the sample is 1.20, and the maximum (1.47) and minimum (0.98) values indicate the model complexity is appropriate for the data quality. We emphasize that the goal of this spectral fitting exercise is not to find the best possible description of each spectrum, but to test if a straightforward model that includes a REXCOR component is a satisfactory description of the data. The χ^2 values obtained here clearly show that this is the case for all 34 observations.

We find that 10 of the 34 observations do not require a warm absorber component, but Mrk 335 and NGC 4593 are best fit with two warm absorbers, similar to the results of earlier studies (e.g. Longinotti et al. 2013; Ursini et al. 2016). Interestingly, the AGN with the largest estimated Eddington ratio (RE 1034+396, $\lambda_{obs} = 1.691$) is the only source that does not need a *xillver* component in the best-fitting model.

[5]A search for correlations with the black hole mass or the estimated physical accretion rate ($\dot{M}$) did not yield any statistically significant relationships.

Nine of the 14 AGNs exhibit narrow residuals below 1 keV after fitting with our baseline model. In these cases, Gaussian components are added to the model to account for these residuals. These components are only added if the improvement is significant at >99.9 pre cent confidence as measured by the F-test. The centroid energies of the Gaussians correspond to emission lines from highly ionized C, N, and O (e.g. N VII at ≈0.5 keV or N VI at ≈0.43 keV). For almost all observations a single Gaussian is added, but in two observations of UGC 3973 we find that two emission lines improve the fit. In one case (1H 0419−577), a Gaussian absorption line at 0.62 keV (likely a blend of O VII and O VIII lines) improves the fit rather than the addition of a second warm absorber. The fit statistic is found to be acceptable after the inclusion of these Gaussians, so further components are not added even if the residuals may indicate the presence of additional features (Fig. B1). Although these Gaussians are added to account for clear residuals in the data, they span such a small range of energies that their presence does not influence the best-fitting REXCOR parameters.

In all cases the added Gaussians are narrow indicating they arise from more distant ionized gas than considered by REXCOR. Our spectral model only includes two sources of emission for photoionized gas – one REXCOR and one *xillver* component. Given the likely complexity of ionized gas around AGNs, it is not surprising that these two models cannot entirely account for all the emission from ionized gas in the observed spectra. Allowing for non-solar abundances may also account for some of these residuals, although, apart from Fe, relaxing this assumption is not possible in *xillver* and the abundances in the REXCOR models are currently fixed at solar. Non-solar abundances, as well as allowing changes in the inclination angle and high-energy cut-off, may also improve the fits at higher energies ($\gtrsim$7 keV) for several sources; however, the key REXCOR parameters (h_f and τ) are largely determined by the soft excess size and shape and so the impact of these high-energy residuals will be minor.

4.2 Relationships with Eddington ratio

The successful REXCOR fits described above give estimates for how the accretion energy in our sample of AGNs is distributed between the disc, a warm corona, and the hot, X-ray emitting corona. It is therefore interesting to consider how changes in the Eddington ratio of the AGNs will impact the flow of accretion energy dissipated in the system. We also include in this analysis the mean values of the REXCOR parameters found by Xiang et al. (2022) when fitting five joint *XMM–Newton/NuSTAR* observations of the quasar HE 1143−1820 with the $h = 20$ REXCOR models. The statistical analysis is performed using Kendall's τ correlation coefficient as implemented in PYMCCORRELATION (Isobe et al. 1986; Privon et al. 2020) with results summarized in Table 2. To compute the correlation coefficient and p-value uncertainties, we take the largest of the two error bars on each data point and assume a symmetric Gaussian distribution about the data that is then sampled 10^4 times. For data pegged at the upper or lower bounds of our parameter space, the single error bar is used to define the symmetric distribution.

Fig. 1 plots f_X, the fraction of accretion energy dissipated in the X-ray emitting hot corona, against λ_{obs} for all observations in the sample. Each AGN is shown with a different colour with individual observations separated by symbol shape. A clear correlation is seen in the figure with Kendall's $\tau = -0.57^{+0.06}_{-0.05}$, which corresponds to a p-value of $1.6^{+16}_{-1.4} \times 10^{-6}$ and indicates a statistically significant

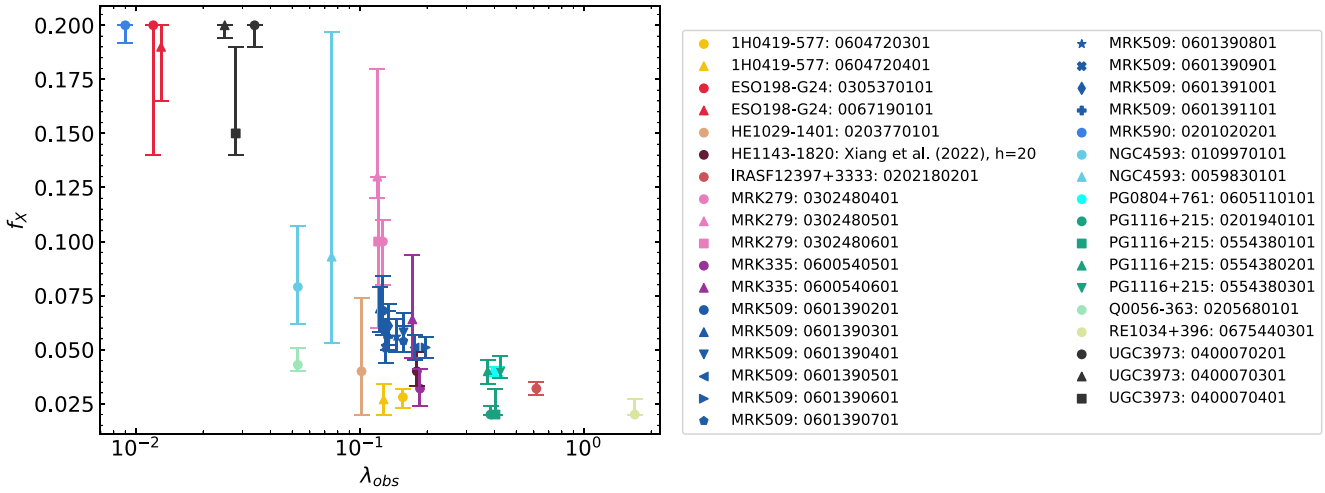

Figure 1. The hot corona heating fraction f_X versus the observed Eddington ratio λ_{obs} as determined from fitting the REXCOR spectral model to the AGN sample listed in Table 1. Each symbol on the plot shows the result from fitting one *XMM–Newton* spectrum, and multiple observations of the same AGN have symbols with the same colour. The f_X parameter is a measure of the fraction of the accretion power dissipated in the lamppost corona. The REXCOR fits (given in Tables A1–A3 and shown in Fig. B1) result in a clear anticorrelation between f_X and λ_{obs}, with Kendall's $\tau = -0.57^{+0.06}_{-0.05}$ (a p-value of $1.6^{+16}_{-1.4} \times 10^{-6}$). This result is consistent with the well-established decrease in X-ray power with λ_{obs} as measured by bolometric corrections (e.g. Vasudevan & Fabian 2009; Duras et al. 2020).

anticorrelation (Table 2).[6] Physically, this relationship shows that the fraction of accretion power released in the hot, X-ray emitting corona drops from $\gtrsim$20 per cent when $\lambda_{obs} \sim 0.01$ to $\lesssim$5 per cent when $\lambda_{obs} \gtrsim 0.2$ (e.g. Kubota & Done 2018). Although the range of f_X provided by REXCOR limits a quantitative comparison, these values and the corresponding relationship are very similar to the ones found in studies of how the X-ray bolometric correction changes with Eddington ratio (e.g. Vasudevan & Fabian 2009; Duras et al. 2020). The fact that fits with the REXCOR model naturally leads to this relationship from our AGN sample suggesting that REXCOR may realistically describe how the distribution of energy changes with λ_{obs}.

The REXCOR fit results lead to a second relationship between the X-ray spectrum and λ_{obs} that has been previously discussed in the literature. Fig. 2 shows that the X-ray photon index Γ found by the REXCOR fits tends to increase with Eddington ratio (e.g. Brandt, Mathur & Elvis 1997; Shemmer et al. 2006, 2008; Risaliti, Young & Elvis 2009; Brightman et al. 2013; Ricci et al. 2013; Trakhtenbrot et al. 2017; Tortosa et al. 2023). As can be seen in the plot, the strength of this relationship is weaker than the f_X one with Kendall's $\tau = 0.26 \pm 0.06$ (a p-value of $3.1^{+6.3}_{-2.3} \times 10^{-2}$; Table 2). The large degree of scatter seen in the figure is similar to that found by other authors (e.g. Fanali et al. 2013; Trakhtenbrot et al. 2017; Diaz et al. 2023), and is a natural outcome of the origin of the power law in a dynamic, Comptonizing corona (Ricci et al. 2018). Fitting a linear function to the data ($\Gamma = \psi \log \lambda_{obs} + b$) yields $\psi = 0.099 \pm 0.038$ and $b = 1.89 \pm 0.04$, consistent with earlier measurements (Ricci et al. 2013; Trakhtenbrot et al. 2017; Tortosa et al. 2023). This result, along with the f_X–λ_{obs} correlation shown in Fig. 1, together shows the applied spectral model, built around a REXCOR component, gives a description of the hard X-ray spectrum of AGNs in agreement with ones found by previous phenomenological models.

[6]In contrast, f_X and the 0.3–10 keV luminosity of the power law ($\log L_{pl}$) are only modestly correlated with Kendall's $\tau = -0.37^{+0.07}_{-0.06}$ and p-value $= 0.0017^{+0.0093}_{-0.0015}$. Thus, the fraction of accretion energy dissipated in the hot corona does not appear to simply translate to the power-law luminosity, but is more dependent on the Eddington ratio of the system.

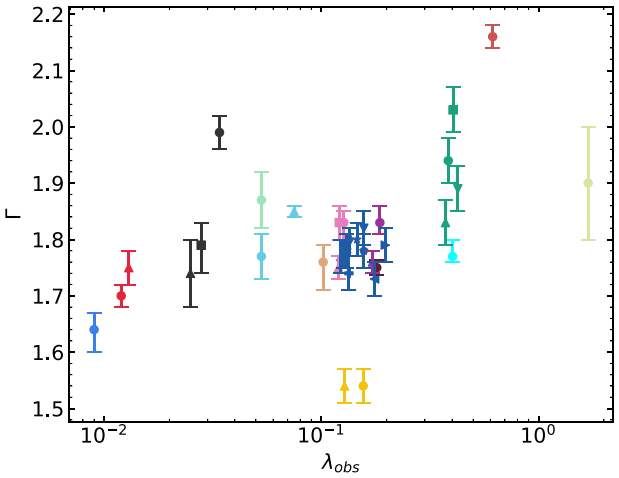

Figure 2. The relationship between the AGN photon index Γ and Eddington ratio λ_{obs} as found from the REXCOR fits (Table A1). The symbols are the same as in Fig. 1. A moderately significant correlation is found between Γ and λ_{obs} (Kendall's $\tau = 0.26 \pm 0.06$, with a p-value of $3.1^{+6.3}_{-2.3} \times 10^{-2}$). The slope of the Γ–log λ correlation is 0.099 ± 0.038, consistent with previous measurements (e.g. Ricci et al. 2013; Trakhtenbrot et al. 2017; Tortosa et al. 2023).

Now that we have demonstrated that the fits recover prior results on the X-ray characteristics of AGNs, we consider the warm corona parameters in the REXCOR model and how these change with λ_{obs}. Fig. 3 plots the optical depth τ and heating fraction h_f of the warm corona as functions of λ_{obs}. A key initial finding is that 33 out of the 34 AGN observations (in addition to the results from HE 1143−1820 from Xiang et al. 2022) are fit with h_f significantly greater than zero with the average $h_f = 0.51$. This fact suggests that a warm corona appears to be a common element of the accretion discs in the AGNs that comprise our sample, with ≈50 per cent of the accretion power

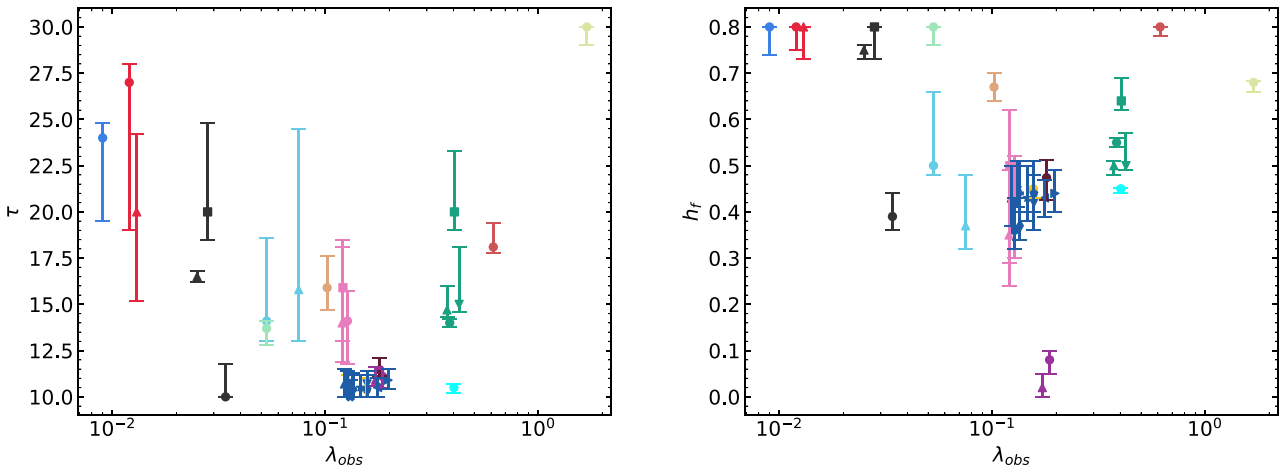

Figure 3. The left panel shows the warm corona optical depth τ found from the REXCOR fits plotted against the observed Eddington ratio λ_{obs} of our AGN sample (Table A1). The right panel plots the fraction of the accretion flux dissipated in the warm corona h_f versus λ_{obs}. The symbols in both panels are the same as in Fig. 1. Aside from one observation of Mrk 335 (Obs ID 0600540601), all fits give a h_f significantly greater than zero, indicating that heating in the warm corona may be important for almost all AGNs in the sample. In both panels, we see evidence for a transition from an anticorrelation with λ_{obs} to a correlation with λ_{obs} at $\lambda_{obs,t} \approx 0.15$ (Table 2).

released in the warm corona. The mean optical depth of the warm corona is $\tau = 14.4$, consistent with values found with fits using phenomenological models (e.g. Jin et al. 2012; Petrucci et al. 2013, 2018; Yu et al. 2023).

Unlike with f_X and Γ, there is clearly no correlation of h_f and τ across the sampled range of λ_{obs}. Rather, there is evidence that both parameters show a 'v'-like shape that appears to transition from an anticorrelation to a correlation between $\lambda_{obs} \approx 0.1$ and 0.2. This 'v' shape is most easily seen in the τ–λ_{obs} panel, but its presence in the h_f–λ_{obs} plot is supported by the significant correlation we find between h_f and τ (Kendall's $\tau = 0.42^{+0.07}_{-0.08}$, p-value $= 4.5^{+39}_{-4.2} \times 10^{-5}$), which suggest that h_f could follow the same trend with λ_{obs}. Based on this shape, we search for a transition $\lambda_{obs,t}$ where both h_f and τ are individually anticorrelated with λ_{obs} below this value and correlated with λ_{obs} above it. We consider $\lambda_{obs,t} = 0.10$, 0.12, 0.15, and 0.2 and average the four p-values that result from Kendall's test for each value of $\lambda_{obs,t}$. A clear minimum[7] is found with $\lambda_{obs,t} = 0.15$ with an average p-value$= 4.6^{+15}_{-3.4} \times 10^{-3}$ (Table 2). The next largest average p-value is 10× greater and occurs when $\lambda_{obs,t} = 0.12$. Thus, there is potentially a significant change in the relationship of the warm corona with λ_{obs} at $\lambda_{obs,t} = 0.15$. The implications of this result are discussed in detail in Section 5.

Fig. 4 shows one other significant correlation that arises from the spectral fits: the REXCOR to power law 0.3–10 keV flux ratio increases with λ_{obs} (Kendall's $\tau = 0.55 \pm 0.03$; p-value $= 3.2^{+7.5}_{-2.2} \times 10^{-6}$; Table 2). Removing RE 1034+396 at $\lambda_{obs} = 1.691$ from the sample only reduces Kendall's τ to 0.53 ± 0.03 and the correlation remains significant (p-value $= 1.3^{+3}_{-0.9} \times 10^{-5}$; Table 2). The flux ratio increases by a factor of ≈5 between $\lambda_{obs} \approx 0.01$ and 0.1 and then rises more gradually. The strengthening of the REXCOR component relative to the power law is consistent with the increase in the strength of the soft excess with λ_{obs} observed (with significant scatter) in Seyfert galaxies (e.g. Gliozzi & Williams 2020; Waddell & Gallo 2020; Yu et al. 2023). Interestingly, the rise in the relative strength

[7]These results are unchanged if the two Mrk 335 observations are removed from the analysis (Table 2).

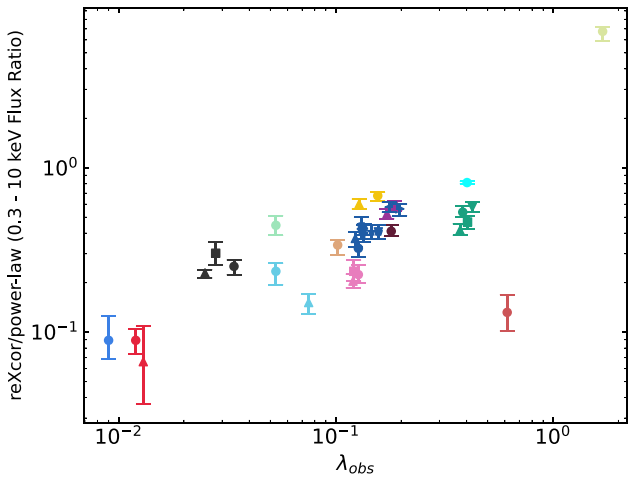

Figure 4. The ratio of the 0.3–10 keV REXCOR and power-law fluxes obtained from the best fits (Table A1) as a function of λ_{obs}. A significant correlation is found between these two quantities with a p-value of $3.2^{+7.5}_{-2.2} \times 10^{-6}$ (Kendall's $\tau = 0.55 \pm 0.03$; Table 2). The correlation persists even after removing the RE 1034+396 point at $\lambda_{obs} = 1.691$. In this case, the p-value increases to $1.3^{+3}_{-0.9} \times 10^{-5}$. The increase in the REXCOR component relative to the intrinsic power law is consistent with the observed strengthening of the soft excess in AGNs with higher Eddington ratios (e.g. Gliozzi & Williams 2020; Waddell & Gallo 2020; Yu et al. 2023).

of REXCOR happens over the entire range of λ_{obs} even though h_f, the fraction of accretion energy released in the warm corona, reaches a minimum at $\lambda_{obs} \approx 0.1$–0.2 (Fig. 3, right). Section 5 presents the interpretation of the increasing flux ratio, along with the changes in τ and h_f, in the context of AGN warm coronae.

5 DISCUSSION

The 34 *XMM–Newton* AGN observations considered in this paper (Table 1) are all well fit with a spectral model that utilizes the REXCOR model to account for both the soft excess and relativistic reflection.

Section 4 showed the resulting relationships between the REXCOR parameters (f_X, the hard X-ray heating fraction; τ, the optical depth of the warm corona; and h_f, the heating fraction of the warm corona) and the observed Eddington ratio of the AGNs. Appendix C shows that these relationships are not strongly affected by model-dependent uncertainties and appear to be robust to changes in assumptions regarding λ, h, or a. Below, we discuss the implications of these results for understanding the role of warm coronae in AGN accretion flows.

5.1 The warm corona and the soft excess in AGNs

A basic, yet crucial, result from our analysis is that $h_f \neq 0$ for all AGNs in the sample (Table A1), implying that a warm corona is common in AGNs across a broad range of black hole masses and Eddington ratios (see e.g. Porquet et al. 2024). However, since the mean $h_f = 0.51$ the observed soft excess is not entirely a result of the warm corona as relativistic reflection will also contribute, and, in some cases (e.g. Mrk 335), even dominate the soft excess. It is reasonable to believe that modelling of the soft excess in X-ray observations of AGNs may require both a warm corona and relativistic reflection (e.g. Porquet et al. 2018, 2021; Xu et al. 2021b). Our results naturally agree with this approach, as both warm corona emission and relativistic reflection are included in REXCOR by construction. Since both f_X and h_f appear to increase toward small λ_{obs}, the fraction of accretion energy dissipated in the disc is lowest for $\lambda_{obs} \sim 0.01$. The REXCOR results for AGNs with higher λ_{obs} suggest that the accretion energy is distributed more evenly between the disc and the two coronae with the disc contributing the largest fraction at $\lambda_{obs} \approx 0.1$–$0.2$.

Recently, Gronkiewicz et al. (2023) developed a one-dimensional theoretical model of an AGN warm corona that includes magnetic heating and pressure support, Compton and free–free cooling, and the effects of radiation and gas pressure. Gronkiewicz et al. (2023) showed that a stable warm corona can develop on the surfaces of AGN accretion discs and how their properties depend on the accretion rate and magnetic properties of the disc. Specifically, the model predicts that the optical depth of the warm corona increases either with the accretion rate or with the strength of the magnetic viscosity. The amount of energy released in the warm corona (similar to REXCOR's h_f) is predicted to reduce with weaker magnetic viscosity, but also be at its highest value for lower accretion rates.

The most intriguing aspect of the spectral fitting results shown in Section 4.2 is that the optical depth and heating fraction of the warm corona may potentially transition from decreasing to increasing with λ_{obs} at $\lambda_{obs,t} \approx 0.15$. Although a direct comparison with the theoretical results of Gronkiewicz et al. (2023) is not possible, the trends seen in Fig. 3 appear to be consistent with the scenario where the strength of the magnetic viscosity in AGN discs is relatively large at low accretion rates but decreases with λ_{obs} until $\lambda_{obs,t} \approx 0.15$, at which point it remains unchanged or only evolves slowly. According to the model of Gronkiewicz et al. (2023), this would explain why τ and h_f are large at low λ_{obs}, drop to a minimum at $\lambda_{obs,t} \approx 0.15$ before increasing with higher accretion rates. Stronger magnetic viscosity at low λ_{obs} could also be a potential explanation for the larger values of f_X in this regime (Fig. 1) as it may lead to increasing magnetic buoyancy (Gronkiewicz et al. 2023) resulting in more efficient heating in the optically thin, X-ray emitting corona.

The increase in the relative strength of the REXCOR component with λ_{obs} (Fig. 4) does not follow any of the correlations of the REXCOR parameters. In particular, although this correlation is consistent with the observed strengthening of the soft excess with λ_{obs} (e.g. Gliozzi & Williams 2020; Waddell & Gallo 2020; Yu et al. 2023), it is not related to the amount of heat dissipated in the warm corona (h_f). One plausible interpretation of the increase in the 0.3–10 keV flux ratio is that it results from a growth in the radial size of the warm corona in the AGN accretion disc. That is, the warm corona spans a small radial range at low λ_{obs} than at large λ_{obs}. A physically smaller warm corona will produce a smaller flux compared to the power law even if it has a large value of h_f, while a warm corona that takes up more area will naturally yield a larger flux compared to the power law. The theoretical model of Gronkiewicz et al. (2023) does predict that the size of a warm corona will increase with accretion rate, which provides some support for this interpretation.

The acceptable spectral fits and the resulting relationships with λ_{obs} show that studying AGNs with models such as REXCOR can produce insight into the energy dissipation processes in the accretion flow. However, more theoretical work is needed in order to provide a clear understanding of the physical processes. While the Gronkiewicz et al. (2023) model suggests a potential interpretation for the behaviours of f_X, τ, and h_f, this will likely be revised as more detailed models are developed. The 'v' shape suggested by Fig. 3 indicates that at least one other physical parameter in addition to λ_{obs} is needed to describe the warm corona heating process. The relatively high degree of scatter observed in all figures also points to a significant amount of object-to-object variability (e.g. the low h_f seen from Mrk 335), which might be expected with such a dynamical environment as a magnetic, radiation-dominated accretion disc. Future REXCOR studies that focus on multiple observations of a single AGN (that ideally span a wide range of λ_{obs}) may be the best strategy for more clearly revealing the relationships affecting the warm and hot coronae in AGNs.

5.2 Coronal height, black hole spin, and Mrk 335

We comment here on three other results that arise from our analysis. First, 21 of the 34 observations produce a constraint on the relative height of the lamppost corona used in the REXCOR model (Table A1). These 21 observations are from 11 individual AGNs, with three sources preferring a 'high' coronal height (1H 0419−577, Mrk 509, and NGC 4593), while six are best fit with a 'low' height (IRASF 12397+3333, ESO 198−G24, Mrk 335, PG 0804+761, Q0056−363, and RE 1034+396) and two AGNs have heights that appear to change between observations (PG 1116+215 and UGC 3973). The six AGNs that prefer the $h = 5$ REXCOR models span a broad range in λ_{obs}, consistent with the results from X-ray reverberation that a low lamppost height may be common across the span of AGN activity (e.g. De Marco et al. 2013; Kara et al. 2016). Recent X-ray polarization measurements from the *Imaging X-ray Polarimetry Explorer* (*IXPE*) suggest a more complex corona geometry in AGNs than an idealized spherical lamppost (e.g. Gianolli et al. 2023). Our results, therefore, may be best interpreted as favouring a geometry where the corona is compact and situated close enough to the black hole that light-bending effects impact the illumination pattern on the disc (e.g. Reis & Miller 2013; Ballantyne 2017).

While the REXCOR fits are able to distinguish between the two values of black hole spin ($a = 0.9$ and 0.99) in 10 AGNs in our sample, these should not be considered as spin measurements for these sources. Xiang et al. (2022) describe a degeneracy between f_X and spin in the REXCOR models, so it is challenging to use REXCOR fits to constrain spin unless the spectrum is strongly affected by relativistic blurring effects. In that case, the difference between the $a = 0.9$ and 0.99 models may be sufficient to distinguish between the two spin values. Mrk 335 is the only AGN in our sample where such

a measurement is plausible as h_f is small enough (Table A1) that the full spectrum, including the soft excess, is predicted to be dominated by relativistic reflection. We find that the REXCOR fits significantly prefer the $a = 0.9$ models over the $a = 0.99$ ones for Mrk 335 (the average $\Delta\chi^2 = +19$ when using the $a = 0.99$ REXCOR model). Keek & Ballantyne (2016) also found a black hole spin of $a \approx 0.9$ for Mrk 335 via multi-epoch spectral fitting of five *XMM–Newton* observations using data only above 3 keV, providing some support for the value of the spin.

Lastly, it is interesting to consider why the two Mrk 335 observations have the lowest values of h_f (indicating a weak, but not absent, warm corona) in the entire sample. These two observations occurred when the AGN was in an 'intermediate' flux state after being in a short-lived 'low' flux state, and were the first X-ray observations of the source to find a multicomponent outflowing warm absorber (Longinotti et al. 2013). It is possible that the accretion disc in Mrk 335 was in a transitory state during these observations as the AGN evolved back to its historical flux level. It is also likely that warm corona properties may exhibit significant object-to-object variability. A future REXCOR analysis of archival Mrk 335 observations would be able to more ably capture the evolution of the warm corona in this source.

Recently, Zoghbi & Miller (2023) estimated that the size of the region producing the soft excess in Mrk 335 is ∼2–4× larger than the hot corona emission region. Although those authors were analysing more recent *Neutron Star Interior Composition Explorer* (*NICER*) data of Mrk 335, their estimated size is consistent with the assumed REXCOR geometry (i.e. a compact hot corona with a radially extended warm corona). While the h_f values are found to be small in these two Mrk 335 observations analysed here, the observed flux ratios are well in the middle of the distribution (Fig. 4). These results support the idea that the size of the warm corona is not strictly determined by the instantaneous energy flux dissipated within the layer, but is rather a function of the overall accretion properties of the system.

5.3 Caveats

The results presented and discussed above are subject to the assumptions and limitations of the REXCOR spectral model. In particular, REXCOR assumes a straightforward lamppost corona that is now disfavoured by *IXPE* observations (e.g. Gianolli et al. 2023), and a constant density warm corona with a fixed heating fraction. The spectral model is limited to only fitting X-ray data. By construction, the accretion disc must always power the lamppost corona and the disc always extends to the ISCO, so f_X can never equal 0 and h_f cannot take arbitrarily large values. In practice, this means that while we can test for the case where the soft excess is entirely the result of relativistic reflection (i.e. $h_f = 0$), we are unable to test for a scenario where there is no relativistic reflection and the warm corona produces the entire soft excess. The REXCOR grids are calculated for only two values of λ while the sample spans a range in λ_{obs} of 188. These caveats must be kept in mind when considering any of our quantitative results (e.g. the mean $h_f = 0.51$). We hope that this work will spur development of new accretion disc–corona models that can relax some of these assumptions.

6 CONCLUSIONS

Unravelling the origin of the soft excess in AGNs is an opportunity to increase our understanding of accretion disc physics using only broad-band X-ray spectroscopy. As the soft excess can be explained by a mix of relativistic reflection and emission from a warm corona, then studying how this combination changes across a broad sample of AGNs should give clues on the flow of accretion energy in the inner disc. In this paper, we report the results of such an experiment. We apply the REXCOR spectral model, which self-consistently includes the effects of both reflection and a warm corona (Xiang et al. 2022), to a sample of 34 *XMM–Newton* observations of 14 type 1 AGNs that span a range of 188 in Eddington ratio and 350 in black hole mass. The fit parameters of the REXCOR model (h_f, the heating fraction of the warm corona; τ, the optical depth of the warm corona; and f_X, the heating fraction of the lamppost corona) have the potential to provide significant insights into the energetics of coronal heating in AGNs.

The key findings of this experiment are as follows.

(i) A basic spectral model that combines REXCOR, a *powerlaw* with cut-offs at low and high energy, and a *xillver* continuum (for distant reflection), all potentially modified by a warm absorber, gives acceptable fits to all 34 observations (with reduced χ^2 between 0.98 and 1.47; Tables A1–A3 and Appendix B). All fits assume solar abundances, a high-energy cut-off energy of 300 keV, and an inclination angle of 30°. The warm corona parameters are largely determined by the soft excess size and shape and will therefore be minimally impacted by these assumptions.

(ii) A significant anticorrelation is found between f_X and λ_{obs}, the estimated Eddington ratio of the AGNs (Fig. 1), indicating that the fraction of accretion energy dissipated in the X-ray emitting corona falls with λ_{obs}. This is consistent with the observed changes in the X-ray bolometric correction (e.g. Duras et al. 2020).

(iii) The photon index and λ_{obs} are correlated with moderate significance (Fig. 2). The slope and intercept of the relationship are consistent with previous measurements (e.g. Tortosa et al. 2023).

(iv) The average value of h_f in the sample is 0.51, which shows that warm corona heating is important for modelling the soft excess in nearly all AGNs in the sample. Only the two Mrk 335 observations have $h_f < 0.1$, indicating that relativistic reflection dominates the soft excess in those observations. Thus, our analysis explicitly demonstrates that the soft excess in AGNs can be successfully modelled by combining the effects of a warm corona with relativistic reflection.

(v) The optical depth τ and heating fraction h_f of the warm corona both show evidence for a 'v'-like relationship with λ_{obs}, transitioning from an apparent anticorrelation to a positive one at $\lambda_{obs,t} \approx 0.15$ (Fig. 3 and Table 2). This result suggests that at least one other physical property, in addition to the Eddington ratio, is important in determining the properties of the warm corona, e.g. the strength of the magnetic viscosity in the disc (Section 5.1; Gronkiewicz et al. 2023).

(vi) The flux of the REXCOR component increases relative to the power law for sources with larger λ_{obs} (Fig. 4), following the known trend for the soft excess to appear stronger in more rapidly accreting AGNs (e.g. Gliozzi & Williams 2020). This can be most readily interpreted as the radial extent of the warm corona increases with λ_{obs}.

(vii) The majority of the AGNs in the sample prefer REXCOR models with a low lamppost height ($h = 5\,r_g$), rather than ones that assume $h = 20\,r_g$ (Section 5.2), indicating that most AGN coronae are compact and lie close to the black hole, regardless of the exact geometry of the corona.

These findings provide strong evidence that both relativistic reflection and a warm corona can accurately describe the soft excess across a range of AGNs. In addition, the REXCOR parameters provide a means by which to study how the accretion energy is distributed in

accretion flows. Future theoretical work on warm coronae is needed to explain the 'v'-shaped relationships between the warm corona properties and the Eddington ratio, as at least one other physical property must be involved. Applying the REXCOR model to a single AGN with multiple high-quality spectra will reduce the effects of object-to-object variability and may clarify some of the relationships presented here. Overall, our results show that careful analysis of the AGN soft excess will yield important new insights into the physics of accretion discs.

ACKNOWLEDGEMENTS

DF participated as part of the Georgia Tech Physics REU program supported by NSF grant no. 1852519. This research was supported by the International Space Science Institute (ISSI) in Bern, through ISSI International Team project #514 (Warm Coronae in AGN: Observational Evidence and Physical Understanding). SB acknowledges support from the EU grant AHEAD-2020 (GA no. 871158). BDM acknowledges support via RYC2018-025950-I, PID2020-117252GB-I00, PID2022-136828NB-C44, and SGR-386/2021. AR and BP were supported by the Polish National Science Center grants no. 2021/41/B/ST9/04110.

DATA AVAILABILITY

The data underlying this article will be shared on reasonable request to the corresponding author. The REXCOR models are publicly available through the XSPEC website.

REFERENCES

Alston W. N. et al., 2020, Nat. Astron., 4, 597
Arnaud K. A., 1996, in Jacoby G. H., Barnes J., eds, ASP Conf. Ser. Vol. 101, Astronomical Data Analysis Software and Systems V. Astron. Soc. Pac., San Francisco, p. 17
Ballantyne D. R., 2017, MNRAS, 472, L60
Ballantyne D. R., 2020, MNRAS, 491, 3553
Ballantyne D. R., Xiang X., 2020, MNRAS, 496, 4255
Bianchi S., Guainazzi M., Matt G., Fonseca Bonilla N., Ponti G., 2009, A&A, 495, 421
Brandt W. N., Mathur S., Elvis M., 1997, MNRAS, 285, L25
Brightman M. et al., 2013, MNRAS, 433, 2485
Crummy J., Fabian A. C., Gallo L., Ross R. R., 2006, MNRAS, 365, 1067
Czerny B., Nikołajuk M., Różańska A., Dumont A. M., Loska Z., Zycki P. T., 2003, A&A, 412, 317
Dauser T., Garcia J., Wilms J., Böck M., Brenneman L. W., Falanga M., Fukumura K., Reynolds C. S., 2013, MNRAS, 430, 1694
De Marco B., Ponti G., Cappi M., Dadina M., Uttley P., Cackett E. M., Fabian A. C., Miniutti G., 2013, MNRAS, 431, 2441
Detmers R. G. et al., 2011, A&A, 534, A38
Diaz Y. et al., 2023, A&A, 669, A114
Duras F. et al., 2020, A&A, 636, A73
Fabian A. C., Ross R. R., 2010, Space Sci. Rev., 157, 167
Fabian A. C., Lohfink A., Kara E., Parker M. L., Vasudevan R., Reynolds C. S., 2015, MNRAS, 451, 4375
Fabian A. C., Lohfink A., Belmont R., Malzac J., Coppi P., 2017, MNRAS, 467, 2566
Fanali R., Caccianiga A., Severgnini P., Della Ceca R., Marchese E., Carrera F. J., Corral A., Mateos S., 2013, MNRAS, 433, 648
Frank J., King A., Raine D. J., 2002, Accretion Power in Astrophysics, 3rd edn. Cambridge Univ. Press, Cambridge
Fukumura K., Kazanas D., 2007, ApJ, 664, 14
Galeev A. A., Rosner R., Vaiana G. S., 1979, ApJ, 229, 318
García J., Kallman T. R., 2010, ApJ, 718, 695
Gianolli V. E. et al., 2023, MNRAS, 523, 4468
Gliozzi M., Williams J. K., 2020, MNRAS, 491, 532
Gronkiewicz D., Różańska A., 2020, A&A, 633, A35
Gronkiewicz D., Różańska A., Petrucci P.-O., Belmont R., 2023, A&A, 675, A198
Haardt F., Maraschi L., 1991, ApJ, 380, L51
Haardt F., Maraschi L., 1993, ApJ, 413, 507
HI4PI Collaboration, 2016, A&A, 594, A116
Isobe T., Feigelson E. D., Nelson P. I., 1986, ApJ, 306, 490
Jiang Y.-F., Blaes O., Stone J. M., Davis S. W., 2019, ApJ, 885, 144
Jin C., Ward M., Done C., Gelbord J., 2012, MNRAS, 420, 1825
Kaastra J. S. et al., 2014, A&A, 570, A73
Kara E., Alston W. N., Fabian A. C., Cackett E. M., Uttley P., Reynolds C. S., Zoghbi A., 2016, MNRAS, 462, 511
Keek L., Ballantyne D. R., 2016, MNRAS, 456, 2722
Kubota A., Done C., 2018, MNRAS, 480, 1247
Liddle A. R., 2004, MNRAS, 351, L49
Longinotti A. L. et al., 2013, ApJ, 766, 104
Magdziarz P., Blaes O. M., Zdziarski A. A., Johnson W. N., Smith D. A., 1998, MNRAS, 301, 179
Martocchia A., Matt G., 1996, MNRAS, 282, L53
Matt G., Perola G. C., Piro L., 1991, A&A, 247, 25
Merloni A., Fabian A. C., 2001, MNRAS, 321, 549
Middei R. et al., 2018, A&A, 615, A163
Middei R. et al., 2019, MNRAS, 483, 4695
Middei R. et al., 2020, A&A, 640, A99
Mukherjee S., Feigelson E. D., Jogesh Babu G., Murtagh F., Fraley C., Raftery A., 1998, ApJ, 508, 314
Mushotzky R. F., Done C., Pounds K. A., 1993, ARA&A, 31, 717
Petrucci P. O. et al., 2001, ApJ, 556, 716
Petrucci P. O. et al., 2013, A&A, 549, A73
Petrucci P. O., Ursini F., De Rosa A., Bianchi S., Cappi M., Matt G., Dadina M., Malzac J., 2018, A&A, 611, A59
Petrucci P. O. et al., 2020, A&A, 634, A85
Piconcelli E., Jimenez-Bailón E., Guainazzi M., Schartel N., Rodríguez-Pascual P. M., Santos-Lleó M., 2005, A&A, 432, 15
Porquet D. et al., 2018, A&A, 609, A42
Porquet D., Reeves J. N., Grosso N., Braito V., Lobban A., 2021, A&A, 654, A89
Porquet D., Hagen S., Grosso N., Lobban A., Reeves J. N., Braito V., Done C., 2024, A&A, 681, A40
Pringle J. E., 1981, ARA&A, 19, 137
Privon G. C. et al., 2020, ApJ, 893, 149
Reis R. C., Miller J. M., 2013, ApJ, 769, L7
Ricci C., Paltani S., Ueda Y., Awaki H., 2013, MNRAS, 435, 1840
Ricci C. et al., 2017, ApJS, 233, 17
Ricci C. et al., 2018, MNRAS, 480, 1819
Risaliti G., Young M., Elvis M., 2009, ApJ, 700, L6
Różańska A., Malzac J., Belmont R., Czerny B., Petrucci P. O., 2015, A&A, 580, A77
Scepi N., Begelman M. C., Dexter J., 2024, MNRAS, 527, 1424
Schwarz G., 1978, Ann. Stat., 6, 461
Shakura N. I., Sunyaev R. A., 1973, A&A, 500, 33
Shemmer O., Brandt W. N., Netzer H., Maiolino R., Kaspi S., 2006, ApJ, 646, L29
Shemmer O., Brandt W. N., Netzer H., Maiolino R., Kaspi S., 2008, ApJ, 682, 81
Strüder L. et al., 2001, A&A, 365, L18
Svensson R., Zdziarski A. A., 1994, ApJ, 436, 599
Tortosa A. et al., 2023, MNRAS, 519, 6267
Trakhtenbrot B. et al., 2017, MNRAS, 470, 800
Ursini F. et al., 2016, MNRAS, 463, 382
Ursini F. et al., 2018, MNRAS, 478, 2663
Ursini F. et al., 2020, A&A, 634, A92
Vasudevan R. V., Fabian A. C., 2007, MNRAS, 381, 1235
Vasudevan R. V., Fabian A. C., 2009, MNRAS, 392, 1124
Waddell S. G. H., Gallo L. C., 2020, MNRAS, 498, 5207

Walton D. J., Nardini E., Fabian A. C., Gallo L. C., Reis R. C., 2013, MNRAS, 428, 2901
Winter L. M., Veilleux S., McKernan B., Kallman T. R., 2012, ApJ, 745, 107
Xiang X. et al., 2022, MNRAS, 515, 353
Xu X., Ding N., Gu Q., Guo X., Contini E., 2021a, MNRAS, 507, 3572
Xu Y., García J. A., Walton D. J., Connors R. M. T., Madsen K., Harrison F. A., 2021b, ApJ, 913, 13
Yamada S. et al., 2023, ApJS, 265, 37
Yu Z., Jiang J., Bambi C., Gallo L. C., Grupe D., Fabian A. C., Reynolds C. S., Brandt W. N., 2023, MNRAS, 522, 5456
Zoghbi A., Miller J. M., 2023, ApJ, 957, 69

APPENDIX A: BEST-FITTING PARAMETERS

This appendix presents the best-fitting parameters from the AGN sample. The results are presented in three tables, where Table A1 lists the main REXCOR parameters as well as the overall χ^2 of the fit, Table A2 contains the fluxes of the three continuum components in the spectra model as well as details of any additional Gaussian emission lines added to the model, and Table A3 provides the warm absorber parameters.

Table A1. The parameters obtained from the REXCOR component of the best-fitting spectral model: the warm corona heating fraction h_f, the lamppost heating fraction f_X, the optical depth of the warm corona τ, and the photon index Γ. For each AGN we test REXCOR models with black hole spin $a = 0.9$ or 0.99, as well as coronal heights $h = 5\,r_g$ or $20\,r_g$ with the model giving the smallest χ^2 entered in the table. For AGNs with more than one observation, the spin that leads to the lowest χ^2 for the first observation is used for any subsequent observations. A '†' ('∗') symbol by the Observation ID indicates that the fit with the other value of h (a) has a $\Delta\chi^2 < 6$ compared to the tabulated model. A 'p' in the error bar denotes a parameter pegging at the boundary of the REXCOR grid. All observations are fit between 0.3 and 12 keV, except for Mrk 509 that is fit between 0.76 and 12 keV to avoid the complex warm absorber features at lower energies.

Object	Obs ID	a	h (r_g)	h_f	f_X	τ	Γ	χ^2/dof
1H 0419−577	0604720301	0.99	20	$0.45^{+0.03}_{-0.02}$	$0.028^{+0.004}_{-0.005}$	$10.4^{+0.6}_{-0.4p}$	1.54 ± 0.03	332/266
	0604720401	0.99	20	$0.46^{+0.04}_{-0.03}$	0.027 ± 0.007	$10.2^{+1.0}_{-0.2p}$	1.54 ± 0.03	253/259
ESO 198−G24	0305370101	0.99	5	$0.80^{+0p}_{-0.05}$	$0.20^{+0p}_{-0.06}$	$27.0^{+1.0}_{-8.0}$	1.70 ± 0.02	282/271
	0067190101†		5	$0.80^{+0p}_{-0.07}$	$0.19^{+0.01p}_{-0.025}$	$20.0^{+4.2}_{-4.8}$	1.75 ± 0.03	331/252
HE 1029−1401	0203770101†*	0.99	20	0.67 ± 0.03	$0.040^{+0.034}_{-0.020p}$	$15.9^{+1.7}_{-1.2}$	$1.76^{+0.03}_{-0.05}$	313/266
IRASF 12397+3333	0202180201*	0.99	5	$0.80^{+0p}_{-0.02}$	0.032 ± 0.003	$18.1^{+1.3}_{-0.3}$	2.16 ± 0.02	313/238
Mrk 279	0302480401†	0.99	20	$0.44^{+0.08}_{-0.14}$	$0.10^{+0.01}_{-0.02}$	$14.1^{+1.6}_{-2.3}$	$1.83^{+0.02}_{-0.03}$	326/270
	0302480501†		5	$0.35^{+0.14}_{-0.11}$	$0.13^{+0.05}_{-0.01}$	$14.0^{+4.1}_{-1.0}$	1.75 ± 0.02	361/270
	0302480601†		20	$0.50^{+0.12}_{-0.21}$	$0.10^{+0.03}_{-0.04}$	$15.9^{+2.6}_{-4.0}$	1.83 ± 0.03	287/264
Mrk 335	0600540501	0.9	5	$0.08^{+0.02}_{-0.03}$	$0.032^{+0.009}_{-0.008}$	$11.1^{+0.4}_{-0.6}$	$1.83^{+0.03}_{-0.02}$	268/247
	0600540601		5	$0.02^{+0.03}_{-0.02}$	$0.064^{+0.03}_{-0.018}$	$10.9^{+0.7}_{-0.3}$	1.76 ± 0.02	343/256
Mrk 509	0601390201*	0.99	20	$0.36^{+0.07}_{-0.04}$	$0.068^{+0.016}_{-0.011}$	$10.5^{+0.9}_{-0.5p}$	$1.78^{+0.02}_{-0.03}$	269/248
	0601390301*		20	$0.43^{+0.07}_{-0.06}$	$0.069^{+0.010}_{-0.011}$	$10.7^{+0.8}_{-0.7p}$	1.77 ± 0.03	321/250
	0601390401*		20	0.42 ± 0.06	0.058 ± 0.009	$10.7^{+0.7}_{-0.7p}$	1.82 ± 0.03	359/250
	0601390501*		20	0.43 ± 0.04	0.051 ± 0.006	$10.5^{+0.5}_{-0.5p}$	1.73 ± 0.03	367/249
	0601390601*		20	$0.44^{+0.05}_{-0.04}$	0.051 ± 0.005	$10.9^{+0.6}_{-0.5}$	1.79 ± 0.03	305/250
	0601390701†*		20	$0.44^{+0.07}_{-0.04}$	$0.054^{+0.007}_{-0.005}$	$10.4^{+0.8}_{-0.4p}$	1.78 ± 0.03	355/250
	0601390801*		20	$0.43^{+0.07}_{-0.05}$	$0.056^{+0.008}_{-0.007}$	$10.5^{+0.7}_{-0.5p}$	1.80 ± 0.03	326/249
	0601390901*		20	$0.45^{+0.06}_{-0.04}$	$0.051^{+0.013}_{-0.007}$	$10.0^{+0.9}_{-0p}$	1.78 ± 0.03	304/248
	0601391001*		20	$0.37^{+0.06}_{-0.03}$	$0.061^{+0.010}_{-0.009}$	$10.4^{+0.8}_{-0.4p}$	$1.80^{+0.02}_{-0.03}$	275/250
	0601391101*		20	$0.44^{+0.07}_{-0.04}$	$0.056^{+0.012}_{-0.006}$	$10.4^{+0.9}_{-0.4p}$	1.74 ± 0.03	286/247
Mrk 590	0201020201†	0.99	5	$0.80^{+0p}_{-0.06}$	$0.20^{+0p}_{-0.008}$	$24.0^{+0.8}_{-4.5}$	$1.64^{+0.03}_{-0.04}$	256/259
NGC 4593	0109970101†*	0.9	20	$0.50^{+0.16}_{-0.02}$	$0.079^{+0.028}_{-0.017}$	$14.1^{+4.5}_{-1.1}$	1.77 ± 0.04	286/254
	0059830101*		20	$0.37^{+0.11}_{-0.05}$	$0.093^{+0.104}_{-0.040}$	$15.8^{+8.7}_{-2.8}$	1.85 ± 0.01	332/268
PG 0804+761	0605110101	0.99	5	$0.45^{+0.001}_{-0.01}$	0.040 ± 0.002	$10.5^{+0.2}_{-0.3}$	$1.77^{+0.03}_{-0.01}$	260/246
PG 1116+215	0201940101	0.99	20	0.55 ± 0.01	$0.020^{+0.004}_{-0p}$	14.0 ± 0.2	1.94 ± 0.04	302/260
	0554380101†		20	$0.64^{+0.05}_{-0.02}$	$0.020^{+0.012}_{-0p}$	$20.0^{+3.3}_{-1.0}$	2.03 ± 0.04	326/246
	0554380201†		5	$0.50^{+0.01}_{-0.02}$	$0.040^{+0.005}_{-0.006}$	$14.7^{+1.3}_{-0.4}$	1.83 ± 0.04	284/248
	0554380301†		5	$0.50^{+0.07}_{-0.01}$	$0.040^{+0.007}_{-0.003}$	$15.0^{+3.1}_{-0.4}$	1.89 ± 0.04	302/237
Q0056−363	0205680101	0.99	5	$0.80^{+0p}_{-0.04}$	$0.043^{+0.008}_{-0.003}$	$13.7^{+0.4}_{-0.9}$	1.87 ± 0.05	300/242
RE 1034+396	0675440301	0.99	5	$0.68^{+0.004}_{-0.02}$	$0.020^{+0.007}_{-0p}$	30^{+0p}_{-1}	1.9 ± 0.1	206/143
UGC 3973	0400070201	0.99	5	$0.39^{+0.05}_{-0.03}$	$0.20^{+0p}_{-0.010}$	$10.0^{+1.8}_{-0p}$	1.99 ± 0.03	286/255
	0400070301†		5	$0.75^{+0.01}_{-0.02}$	$0.20^{+0p}_{-0.006}$	16.5 ± 0.3	1.74 ± 0.06	270/246
	0400070401†		20	$0.80^{+0p}_{-0.07}$	$0.15^{+0.04}_{-0.01}$	$20.0^{+4.8}_{-1.5}$	$1.79^{+0.04}_{-0.05}$	248/244

Table A2. In this table, we provide the 0.3–10 keV fluxes (F, in erg cm^{-2} s^{-1}) of the REXCOR, *powerlaw*, and *xillver* components from the best-fitting models in Table A1. The fluxes are determined using the 'cflux' command in XSPEC. RE 1034+396 did not require a *xillver* contribution to the best-fitting model. In addition, the energy (E, in keV) and normalization (K, in photons cm^{-2} s^{-1}) of any narrow ($\sigma = 0$) Gaussian emission lines added to the model are also tabulated. Most sources only required one line, but UGC 3973 required an additional line. These lines correspond to emission features from highly ionized C, N, and O. Empty entries are denoted with '–'.

Object	Obs ID	log F (REXCOR)	log F (*powerlaw*)	log F (*xillver*)	E (keV)	K ($\times 10^{-5}$)
1H 0419−577	0604720301	$-10.88^{+0.01}_{-0.02}$	-10.71 ± 0.01	<-12.75	0.62 ± 0.01	-27 ± 4
	0604720401	-10.95 ± 0.02	-10.73 ± 0.01	<-12.78	0.62 ± 0.01	-19^{+6}_{-7}
ESO 198−G24	0305370101	$-11.83^{+0.06}_{-0.07}$	-10.78 ± 0.01	$-12.27^{+0.06}_{-0.08}$	0.88 ± 0.02	1.3 ± 0.5
	0067190101	$-11.82^{+0.21}_{-0.24}$	-10.64 ± 0.01	$-12.57^{+0.21}_{-0.40}$	0.51 ± 0.02	7.8 ± 2.9
HE 1029−1401	0203770101	$-10.97^{+0.02}_{-0.05}$	-10.50 ± 0.01	$-12.18^{+0.12}_{-0.16}$	0.51 ± 0.01	37 ± 7
IRASF 12397+3333	0202180201	-11.79 ± 0.10	-10.91 ± 0.01	$-12.69^{+0.12}_{-0.21}$	$0.48^{+0.01}_{-0.004}$	16 ± 2
Mrk 279	0302480401	$-10.98^{+0.05}_{-0.04}$	-10.33 ± 0.01	$-11.85^{+0.07}_{-0.08}$	0.47 ± 0.01	44^{+7}_{-6}
	0302480501	$-11.04^{+0.04}_{-0.03}$	$-10.35^{+0.003}_{-0.01}$	-11.88 ± 0.06	0.46 ± 0.01	22^{+12}_{-6}
	0302480601	$-10.99^{+0.06}_{-0.05}$	-10.36 ± 0.01	$-11.80^{+0.08}_{-0.11}$	0.47 ± 0.01	26^{+14}_{-8}
Mrk 335	0600540501	-11.34 ± 0.02	-11.11 ± 0.01	$-12.31^{+0.07}_{-0.08}$	–	–
	0600540601	-11.44 ± 0.02	-11.16 ± 0.01	$-12.47^{+0.07}_{-0.09}$	–	–
Mrk 509	0601390201	$-10.64^{+0.03}_{-0.04}$	-10.15 ± 0.01	$-11.88^{+0.09}_{-0.11}$	–	–
	0601390301	$-10.58^{+0.03}_{-0.04}$	-10.15 ± 0.01	$-11.84^{+0.08}_{-0.09}$	–	–
	0601390401	-10.48 ± 0.03	-10.09 ± 0.01	$-11.76^{+0.07}_{-0.09}$	–	–
	0601390501	-10.46 ± 0.02	-10.22 ± 0.01	$-11.97^{+0.09}_{-0.12}$	–	–
	0601390601	$-10.38^{+0.02}_{-0.03}$	-10.13 ± 0.01	$-11.83^{+0.08}_{-0.10}$	–	–
	0601390701	-10.47 ± 0.03	-10.08 ± 0.01	$-11.82^{+0.08}_{-0.09}$	–	–
	0601390801	-10.49 ± 0.03	-10.10 ± 0.01	$-11.78^{+0.07}_{-0.09}$	–	–
	0601390901	$-10.43^{+0.05}_{-0.06}$	-10.07 ± 0.01	$-11.78^{+0.07}_{-0.09}$	–	–
	0601391001	$-10.51^{+0.02}_{-0.03}$	-10.14 ± 0.01	$-11.79^{+0.07}_{-0.08}$	–	–
	0601391101	-10.49 ± 0.04	-10.09 ± 0.01	$-11.84^{+0.09}_{-0.10}$	–	–
Mrk 590	0201020201	$-12.02^{+0.14}_{-0.10}$	-10.97 ± 0.01	$-12.28^{+0.08}_{-0.09}$	$0.86^{+0.05}_{-0.03}$	1.2 ± 0.5
NGC 4593	0109970101	$-10.80^{+0.03}_{-0.07}$	$-10.17^{+0.02}_{-0.01}$	$-11.64^{+0.10}_{-0.13}$	0.45 ± 0.01	56^{+18}_{-22}
	0059830101	$-10.97^{+0.04}_{-0.06}$	-10.15 ± 0.01	-11.55 ± 0.05	0.46 ± 0.01	47 ± 13
PG 0804+761	0605110101	$-10.88^{+0.004}_{-0.003}$	-10.79 ± 0.004	$-12.39^{+0.12}_{-0.17}$	0.44 ± 0.01	75^{+13}_{-8}
PG 1116+215	0201940101	$-11.47^{+0.03}_{-0.02}$	-11.20 ± 0.01	$-12.74^{+0.11}_{-0.20}$	–	–
	0554380101	-11.35 ± 0.03	-11.02 ± 0.01	$-12.52^{+0.14}_{-0.19}$	–	–
	0554380201	$-11.49^{+0.03}_{-0.02}$	-11.11 ± 0.01	$-12.69^{+0.14}_{-0.26}$	–	–
	0554380301	-11.48 ± 0.02	-11.24 ± 0.01	$-12.61^{+0.13}_{-0.07}$	–	–
Q0056−363	0205680101	-11.64 ± 0.04	-11.29 ± 0.02	$-12.81^{+0.13}_{-0.17}$	–	–
RE 1034+396	0675440301	$-10.85^{+0.01}_{-0.005}$	$-11.68^{+0.02}_{-0.05}$	–	–	–
UGC 3973	0400070201	$-10.96^{+0.03}_{-0.04}$	-10.36 ± 0.01	$-11.87^{+0.10}_{-0.13}$	0.48 ± 0.01	37^{+14}_{-11}
					$0.77^{+0.01}_{-0.004}$	171^{+22}_{-36}
	0400070301	$-11.12^{+0.01}_{-0.02}$	-10.48 ± 0.01	$-11.95^{+0.07}_{-0.08}$	0.77 ± 0.01	43^{+6}_{-11}
	0400070401	$-11.03^{+0.06}_{-0.05}$	$-10.51^{+0.01}_{-0.02}$	$-11.95^{+0.11}_{-0.15}$	0.47 ± 0.01	35^{+11}_{-9}
					$0.77^{+0.02}_{-0.01}$	28^{+71}_{-16}

Table A3. The column density ($N_{\rm H}$ in cm^{-2}) and ionization parameter (ξ, in erg s^{-1} cm^{-1}) of any warm absorber in the best-fitting model (Table A1). Observations that did not require a warm absorber are omitted from the table. Mrk 335 and NGC 4593 both required two warm absorbers. A 'p' in the error bar denotes a parameter pegging at the boundary of the warm absorber grid.

Object	Obs ID	$N_{\rm H}$	$\log \xi$
1H 0419−577	0604720301	$4.6^{+2}_{-1.4} \times 10^{20}$	$0.85^{+0.29}_{-0.49}$
	0604720401	$3.8^{+3.6}_{-1.2} \times 10^{20}$	$0.73^{+0.49}_{-0.73p}$
IRASF 12397+3333	020218201	$6.1^{+0.8}_{-0.6} \times 10^{21}$	1.83 ± 0.02
Mrk 279	0302480401	$2.9^{+1.0}_{-1.1} \times 10^{20}$	$1.68^{+0.08}_{-0.36}$
	0302480501	$1.8^{+0.6}_{-0.5} \times 10^{20}$	$0^{+0.37}_{-0p}$
	0302480601	$1.5^{+0.4}_{-1.5p} \times 10^{20}$	$0.05^{+0.5}_{-0.05p}$
Mrk 335	0600540501	$4.8^{+0.8}_{-0.9} \times 10^{21}$	1.89 ± 0.03
		$1.1^{+3.6}_{-0.8} \times 10^{22}$	$2.91^{+0.25}_{-0.17}$
	0600540601	$1.1^{+0.1}_{-0.1} \times 10^{22}$	$1.87^{+0.03}_{-0.01}$
		$1.3^{+1}_{-0.9} \times 10^{22}$	$2.86^{+0.06}_{-0.13}$
Mrk 509	0601390901	$1.1^{+1.0}_{-0.7} \times 10^{21}$	$2.03^{+0.22}_{-0.08}$
	0601391101	$6.4^{+4.0}_{-3.3} \times 10^{20}$	$2.26^{+0.28}_{-0.22}$
NGC 4593	0109970101	$3.5^{+4.1}_{-1.2} \times 10^{20}$	$0.50^{+0.58}_{-0.38}$
		$3.8^{+1.2}_{-0.7} \times 10^{21}$	$2.06^{+0.04}_{-0.05}$
	0059830101	$5.4^{+1.2}_{-1.6} \times 10^{20}$	$0.74^{+0.20}_{-0.18}$
		$3.0^{+0.4}_{-0.5} \times 10^{21}$	$2.16^{+0.05}_{-0.08}$
PG 0804+761	0605110101	$1.0^{+0.3}_{-0p} \times 10^{20}$	$0.63^{+0.21}_{-0.63p}$
PG 1116+215	0201940101	$2.6 \pm 0.4 \times 10^{20}$	$0^{+0.13}_{-0p}$
	0554380101	$3.5^{+0.6}_{-0.5} \times 10^{20}$	$0^{+0.11}_{0p}$
	0554380201	$3.1^{+0.5}_{-0.4} \times 10^{20}$	$0^{+0.37}_{-0p}$
	0554380301	$4.1^{+0.5}_{-0.4} \times 10^{20}$	$0^{+0.20}_{-0p}$
Q0056−363	0205680101	$1.0^{+1.0}_{-0p} \times 10^{20}$	$0^{+0.82}_{-0p}$
RE 1034+396	0675440301	$1.0^{+1.3}_{-0p} \times 10^{20}$	$0.21^{+0.31}_{-0.21p}$
UGC 3973	0400070201	$5.2^{+0.3}_{-0.5} \times 10^{21}$	$1.69^{+0.02}_{-0.04}$
	0400070301	$6.0^{+0.2}_{-0.5} \times 10^{21}$	$1.69^{+0.06}_{-0.03}$
	0400070401	$6.1^{+0.9}_{-0.6} \times 10^{21}$	$1.73^{+0.04}_{-0.03}$

APPENDIX B: PLOTS OF BEST FITS

Fig. B1 plots the best-fitting spectrum for each observation using the model described in Section 3. The upper portion of each panel shows the total spectrum (solid line), plus the contributions from the power law (short-dashed line), the REXCOR model (dot–dashed line), and the *xillver* distant reflector (dotted line). Any Gaussian lines are shown as dot–dot–dashed lines. The lower part of each panel plots the residuals from the best-fitting model in units of σ. The parameters of the best-fitting model are listed in Tables A1–A3.

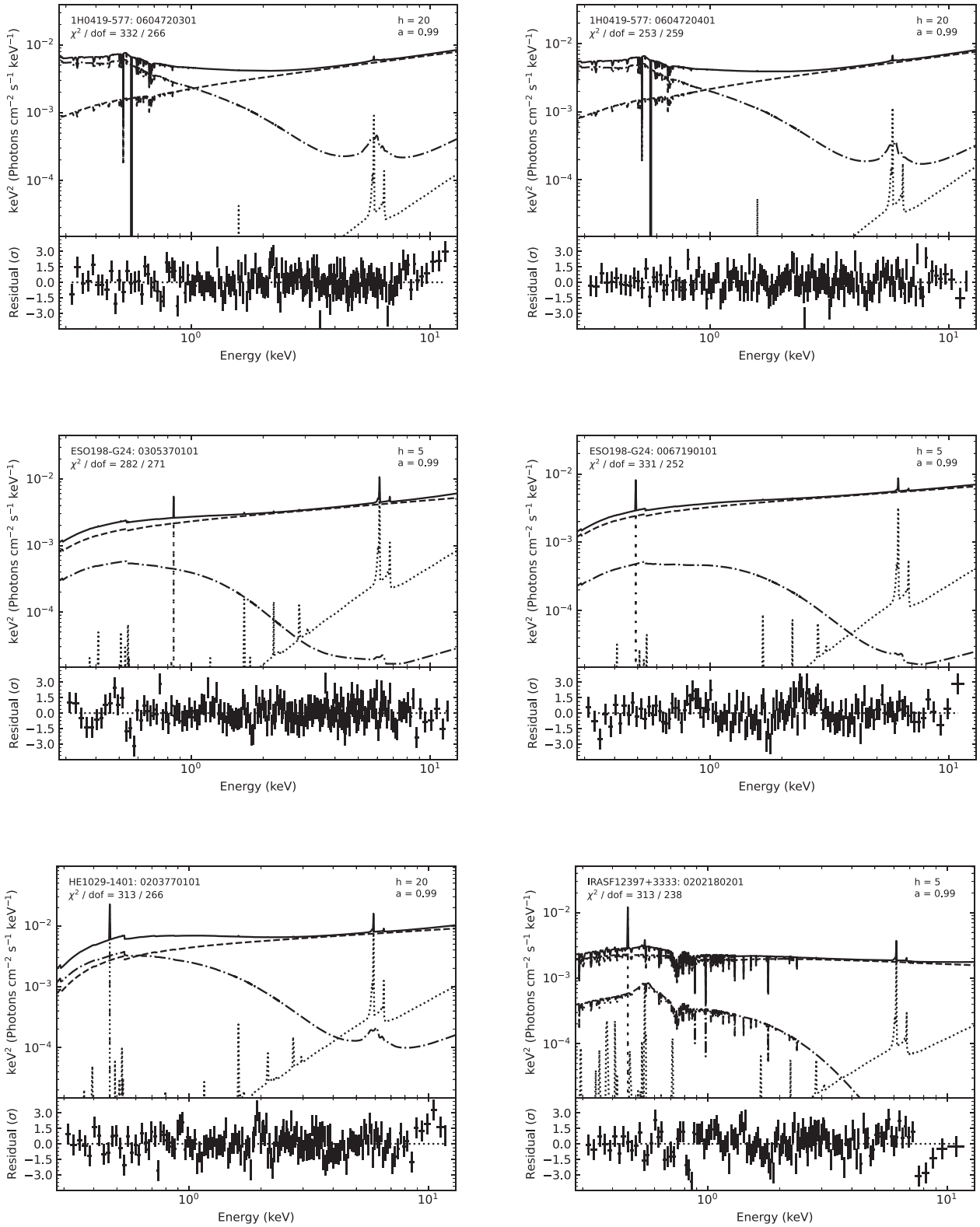

Figure B1. The upper part of each panel plots the spectral model found from the best fit to each observation in our sample (Tables A1–A3). The solid line shows the total model, while the short-dashed, dot–dashed, and dotted lines plot the *powerlaw*, REXCOR, and *xillver* components, respectively. Any Gaussian lines are shown using dot–dot–dashed lines.

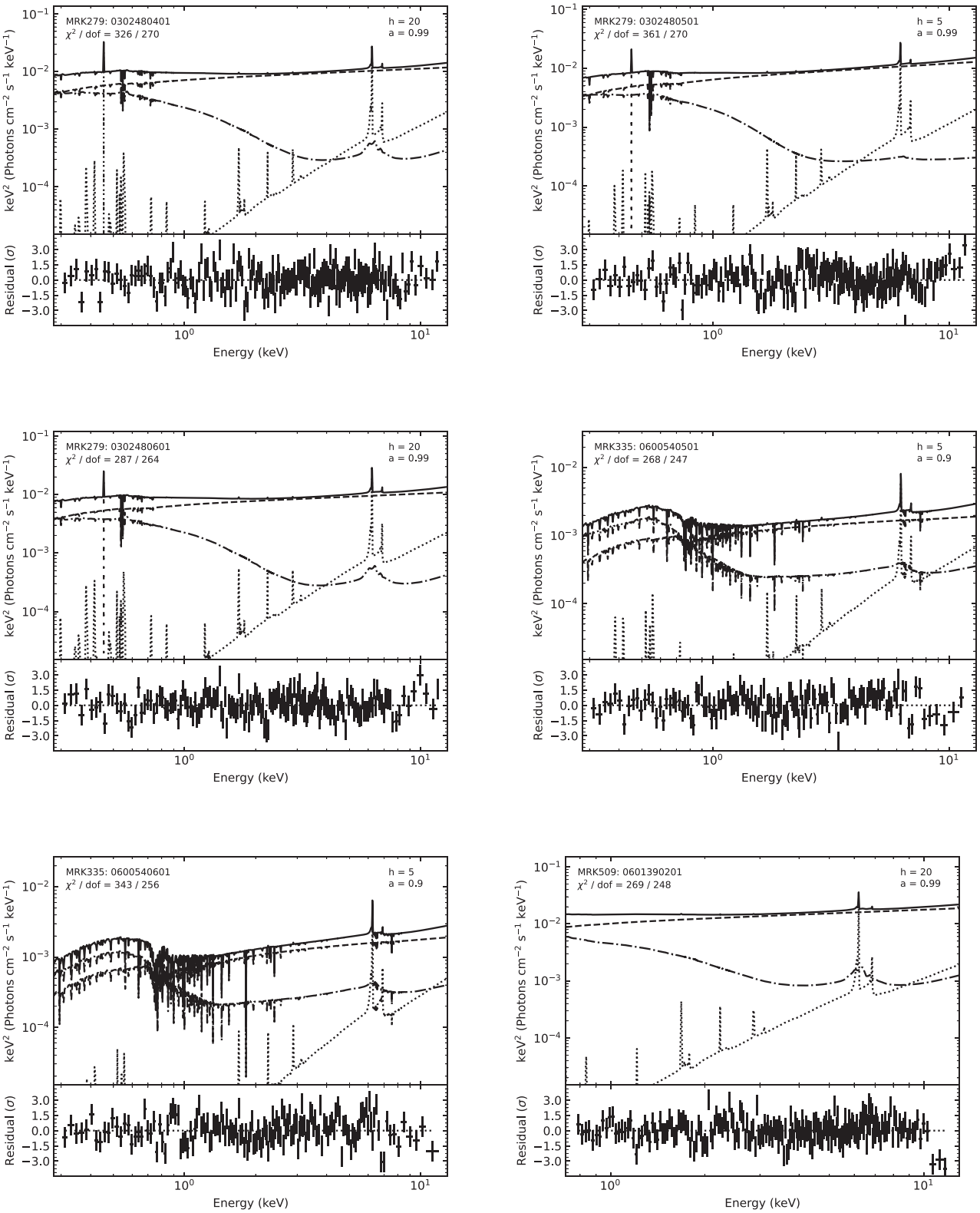

Figure B1. *continued.*

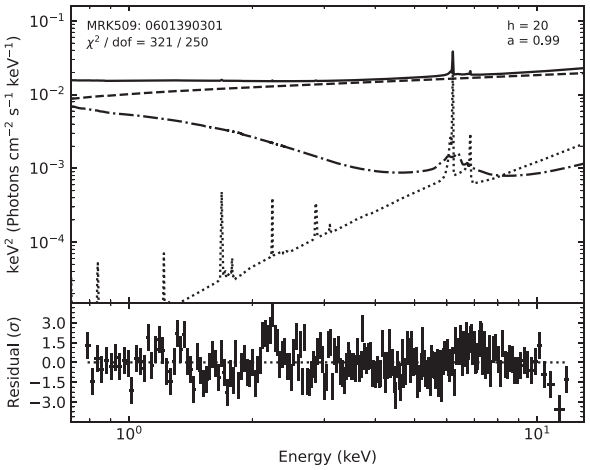

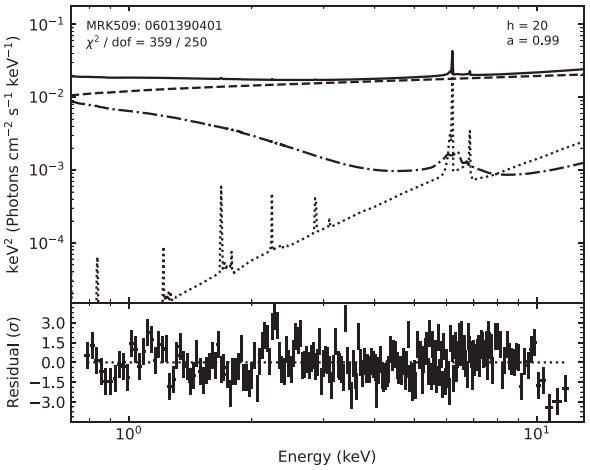

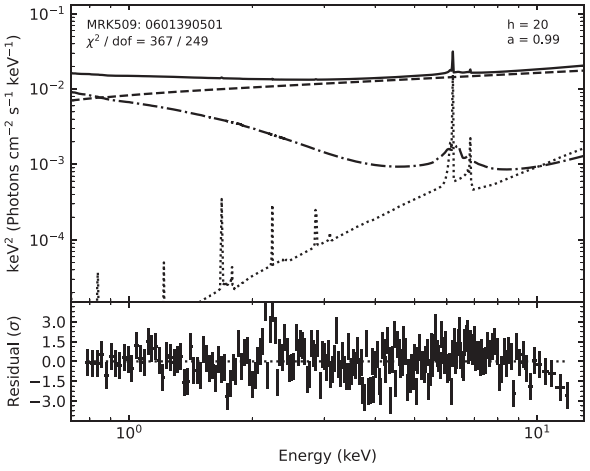

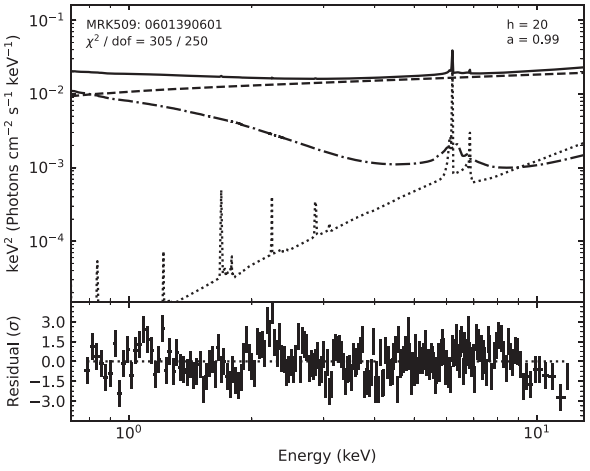

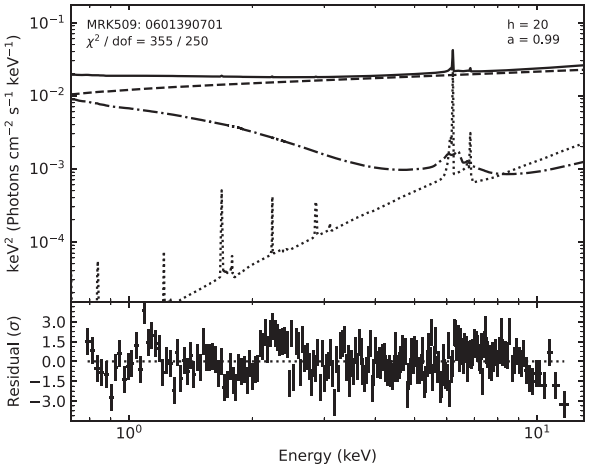

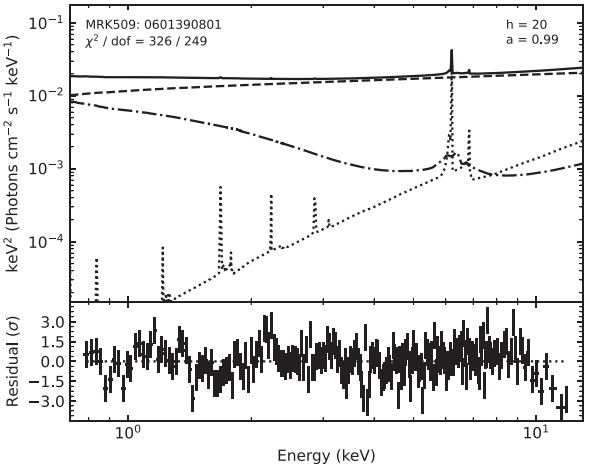

Figure B1. *continued.*

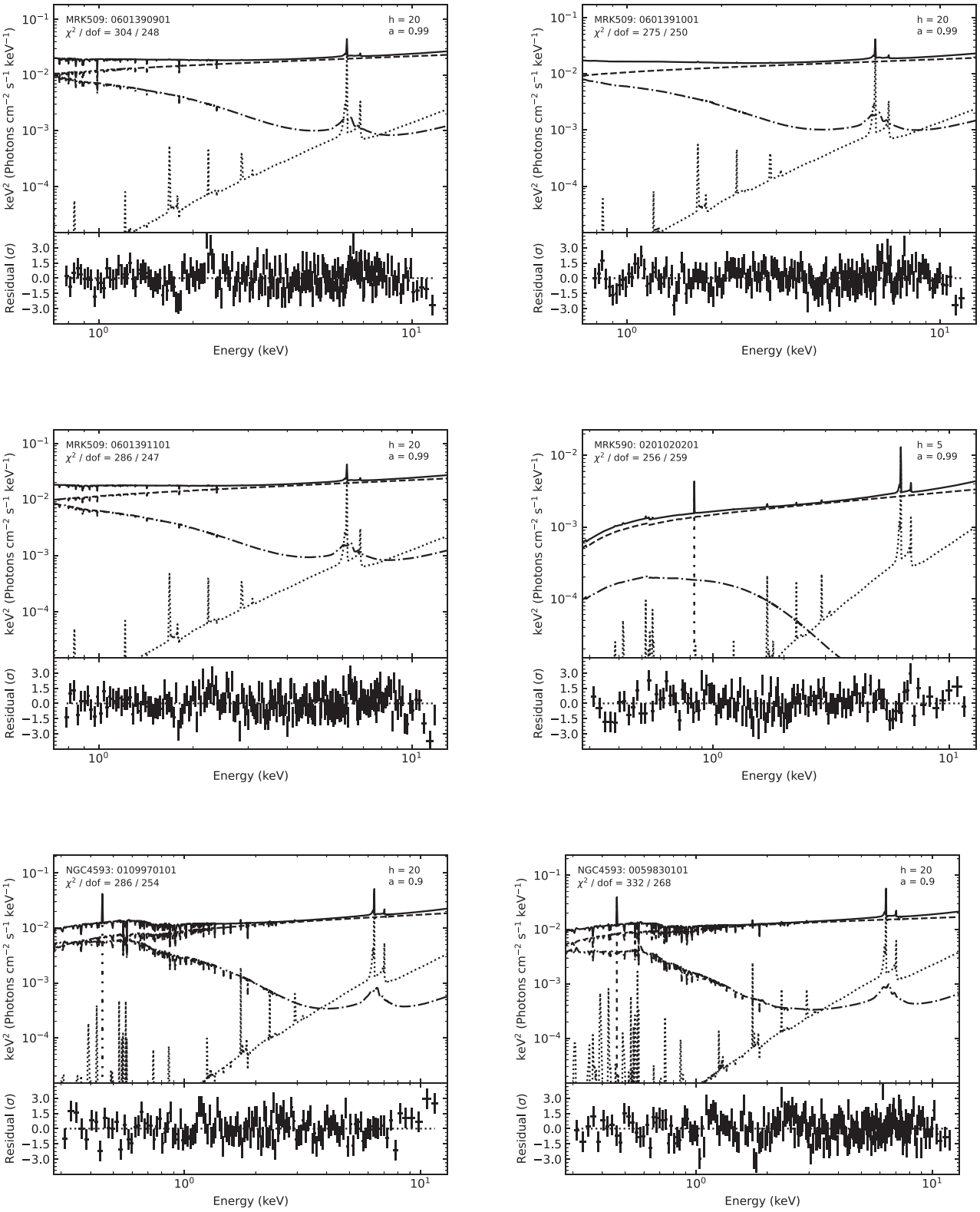

Figure B1. *continued.*

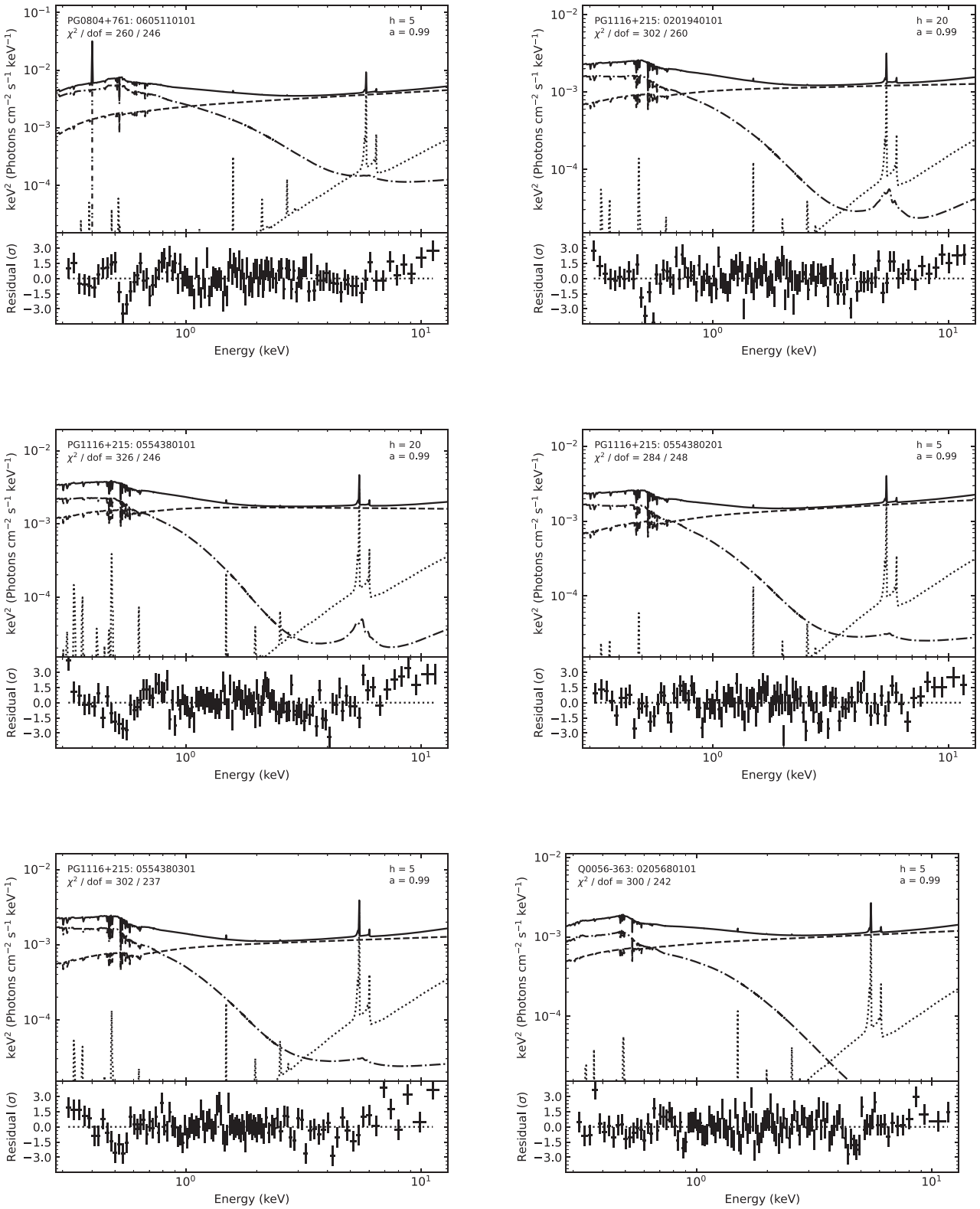

Figure B1. *continued.*

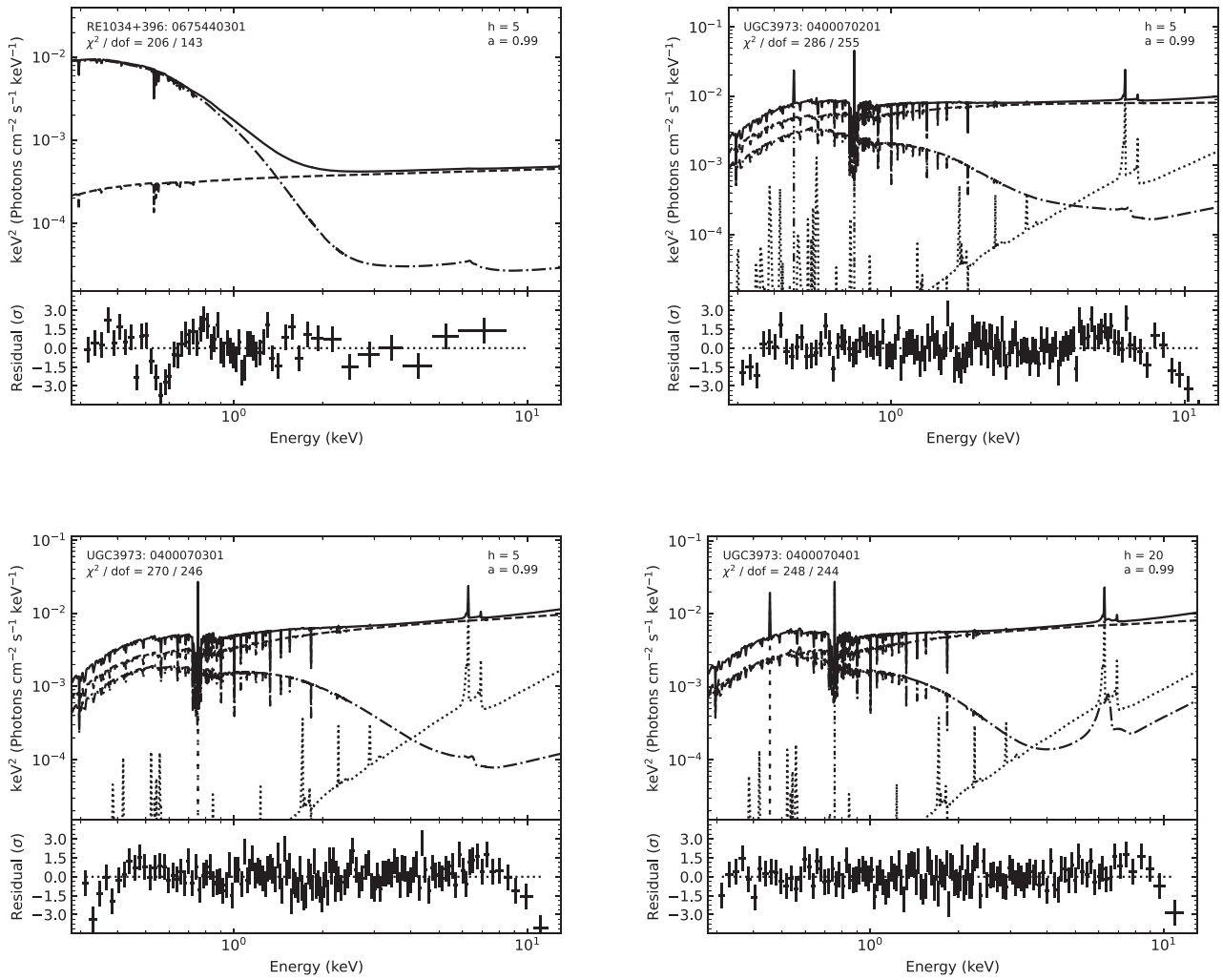

Figure B1. *continued*.

Table C1. As in Table A1, but now showing the results when the $\lambda = 0.1$ REXCOR grids are used when fitting the seven observations of AGNs that were originally fit with $\lambda = 0.01$ REXCOR models. The last column shows the change in χ^2 and degrees of freedom that result from using the $\lambda = 0.1$ REXCOR grids. A 'p' in the error bar denotes a parameter pegging at the boundary of the REXCOR grid.

Object	Obs ID	a	h (r_g)	h_f	f_X	τ	Γ	$\Delta\chi^2/\Delta$dof
ESO 198−G24	0305370101	0.99	5	$0.13^{+0.12}_{-0.04}$	$0.15^{+0.05p}_{-0.03}$	$10.5^{+1.8}_{-0.5p}$	$1.72^{+0.02}_{-0.02}$	−8/0
	0067190101		5	$0.72^{+0.06}_{-0.22}$	$0.20^{+0p}_{-0.09}$	$30.0^{+0p}_{-13.7}$	$1.76^{+0.04}_{-0.03}$	−7/0
Mrk 590	0201020201	0.99	5	$0.02^{+0.06}_{-0.02p}$	$0.20^{+0p}_{-0.04}$	$10.0^{+0.5}_{-0p}$	$1.69^{+0.02}_{-0.03}$	−9/+2
Q0056−363	0205680101	0.99	20	0.55 ± 0.01	$0.020^{+0.008}_{-0p}$	$10.5^{+0.4}_{-0.5p}$	$1.77^{+0.08}_{-0.06}$	+6/0
UGC 3973	0400070201	0.99	20	$0.65^{+0.03}_{-0.09}$	$0.20^{+0p}_{-0.01}$	$27.6^{+0.5}_{-2.2}$	$2.03^{+0.01}_{-0.02}$	−5/0
	0400070301		20	0.71 ± 0.01	$0.20^{+0p}_{-0.05}$	$30.0^{+0p}_{-2.7}$	$1.77^{+0.04}_{-0.03}$	−17/−2
	0400070401		20	$0.32^{+0.26}_{-0.09}$	$0.19^{+0.01p}_{-0.04}$	$13.4^{+4.8}_{-0.3}$	$1.81^{+0.03}_{-0.06}$	+8/0

APPENDIX C: MODEL-DEPENDENT EFFECTS

The results presented in Section 4 focus on the REXCOR parameters related to the distribution of accretion energy. However, the REXCOR models also depend on the assumed Eddington ratio, the height of the hot corona (situated as a 'lamppost' above the black hole), and the spin of the black hole. In this appendix, we discuss how our results may depend on these other parameters.

C1 The Eddington ratio, λ

As mentioned in Section 3, we used the $\lambda = 0.01$ REXCOR grids when fitting observations with $\lambda_{obs} < 0.05$. Following the predictions of standard accretion theory (e.g. Shakura & Sunyaev 2009), the $\lambda = 0.01$ REXCOR models are calculated with a denser accretion disc than the $\lambda = 0.1$ models. This fact, combined with the lower luminosity, predicts a less ionized reflection and emission spectrum for a given

Table C2. As in Table A2, but now showing the results when the $\lambda = 0.1$ REXCOR grids are used when fitting the seven observations that were originally fit with the $\lambda = 0.01$ grids. Note that Mrk 590 no longer requires a Gaussian emission line. The 'f' indicates the line width was fixed at 0 keV.

Object	Obs ID	log F (REXCOR)	log F (*powerlaw*)	log F (*xillver*)	E (keV)	K ($\times 10^{-5}$)	σ (keV)
ESO 198−G24	0305370101	-11.82 ± 0.07	-10.78 ± 0.01	$-12.26^{+0.07}_{-0.08}$	0.50 ± 0.01	$5.1^{+1.8}_{-1.7}$	0^{f}
	0067190101	$-11.91^{+0.12}_{-0.19}$	-10.64 ± 0.01	$-12.57^{+0.20}_{-0.39}$	0.51 ± 0.01	$9.9^{+3.0}_{-3.2}$	0^{f}
Mrk 590	0201020201	$-12.15^{+0.11}_{-0.10}$	-10.97 ± 0.01	$-12.24^{+0.06}_{-0.08}$	–	–	–
Q0056−363	0205680101	$-11.49^{+0.04}_{-0.06}$	$-11.33^{+0.03}_{-0.02}$	$-12.93^{+0.15}_{-0.18}$	–	–	–
UGC 3973	0400070201	$-10.97^{+0.01}_{-0.03}$	-10.34 ± 0.01	$-11.83^{+0.06}_{-0.11}$	0.48 ± 0.01	52^{15}_{-8}	0^{f}
					0.77 ± 0.01	229^{+54}_{-83}	0^{f}
	0400070301	$-11.13^{+0.07}_{-0.04}$	-10.47 ± 0.01	$-11.97^{+0.10}_{-0.14}$	0.50 ± 0.02	18^{+12}_{-7}	0^{f}
					$0.77^{+0.01}_{-0.02}$	132^{+63}_{-16}	0^{f}
	0400070401	$-10.91^{+0.04}_{-0.02}$	$-10.54^{+0.01}_{-0.02}$	$-11.94^{+0.10}_{-0.13}$	0.48 ± 0.01	43^{+12}_{-9}	0^{f}
					0.77 ± 0.01	36^{+20}_{-6}	0^{f}

Table C3. As in Table A3, but now showing the results when the $\lambda = 0.1$ REXCOR grids are used when fitting the seven observations that were originally fit with the $\lambda = 0.01$ models. A '*p*' in the error bar denotes a parameter pegging at the boundary of the warm absorber grid.

Object	Obs ID	$N_{\rm H}$	log ξ
Q0056−363	0205680101	$3.7^{+0.4}_{-0.6} \times 10^{20}$	$0^{+0.16}_{-0p}$
UGC 3973	0400070201	$6.4^{+0.1}_{-0.6} \times 10^{21}$	1.69 ± 0.04
	0400070301	$6.5^{+0.3}_{-0.2} \times 10^{21}$	$1.66^{+0.02}_{-0.12}$
	0400070401	$7.6^{+0.5}_{-0.9} \times 10^{21}$	$1.72^{+0.05}_{-0.03}$

$f_{\rm X}$ and $h_{\rm f}$ (Xiang et al. 2022). Therefore, it is possible that the high values of $h_{\rm f}$ and $f_{\rm X}$ found in observations with $\lambda_{\rm obs} < 0.05$ are just a result of this choice and are not required by the data.

To determine how sensitive the warm corona parameters are to the assumed Eddington ratio of the REXCOR models, we refit all seven observations that were originally fit with the $\lambda = 0.01$ models with the lower density $\lambda = 0.1$ REXCOR grids, and the results are tabulated in Tables C1–C3 that follow the same format as Tables A1–A3. The rightmost column of Table C1 shows the change in χ^2, as well as any difference in the degrees of freedom, when the $\lambda = 0.01$ REXCOR grids are replaced with $\lambda = 0.1$ grids. To determine how significant these different fits are from the original ones, we use the Bayesian information criterion (BIC; Schwarz 1978; Liddle 2004), which for χ^2 statistics is BIC $= \chi^2 + k \ln(N)$, where k is the number of parameters and N is the number of data points (e.g. Yamada et al. 2023). If the ΔBIC between two models is <6, then there is only marginal evidence for one model being preferred over the other (Mukherjee et al. 1998). In all of our cases, N is the same between the two models, and only two observations (Mrk 590 and UGC 3973 [Obs ID 0400070301]) have a different number of parameters. For the remaining five observations the ΔBIC is equivalent to $\Delta\chi^2$.

Examination of Table C1 shows that using the $\lambda = 0.1$ REXCOR grids leads to a larger χ^2 for Q0056−363 and one observation of UGC 3973 (Obs ID 0400070401) compared to the fits using the original $\lambda = 0.01$ grids. According to the ΔBIC criterion, the differences in χ^2 are large enough to conclude that the model in Table A1 is preferred. The remaining five observations all result in a decrease in χ^2 using the $\lambda = 0.1$ grid. Fig. C1 replots the relationships with $\lambda_{\rm obs}$ shown in Section 4 with the REXCOR parameters from these five observations replaced with the values from Table C1.

The most significant change in the REXCOR parameters occurs in the two observations with the lowest $\lambda_{\rm obs}$ in the sample (Mrk 590 and ESO 198−G24 [Obs ID 0305370101]). In both cases, $h_{\rm f}$ and τ fall to much lower values than was originally found with the $\lambda = 0.01$ REXCOR grids. Interestingly, the parameters found in the other ESO 198−G24 observation (Obs ID 0067190101) are consistent with the prior fit, despite having essentially the same $\lambda_{\rm obs}$ (Table 1). If this new fit for Obs ID 0305370101 is a better representation of the coronal properties, then it would imply that AGN coronae can be substantially different in the same object even at approximately the same $\lambda_{\rm obs}$.

The impact of these changes on our statistical analysis is shown in Table C4.

Comparing these values to the ones in Table 2 shows that the three correlations with $\lambda_{\rm obs}$ described in Section 4 are retained here at comparable levels of significance. However, the evidence for 'v'-shaped relationships of τ and $h_{\rm f}$ with $\lambda_{\rm obs}$ is lost unless Mrk 590 and ESO 198−G24 (Obs ID 0305370101) are omitted from the analysis. Therefore, we conclude that the results described in Section 4 are robust to changing the assumed λ in the REXCOR modelling, except at Eddington ratios $\lesssim$0.01. It is possible that at these accretion rates, the disc is transitioning away from an optically thick flow (driven, perhaps, by the unknown second parameter needed to explain the warm corona evolution), and the REXCOR model would no longer be applicable.

For completeness, we also perform the opposite experiment where the 27 observations best fit with the $\lambda = 0.1$ REXCOR grids are refit using the $\lambda = 0.01$ models. A large majority of the 27 observations are poorly fit with these higher density, less ionized models, with the median $\Delta\chi^2 = +19.4$. Only five of the observations have a $\Delta\chi^2 < 6$, with just two of these giving a negative $\Delta\chi^2$: Mrk 279, Obs ID 03022480501 ($\Delta\chi^2 = -0.2$) and PG 1116+215, Obs ID 0554380301 ($\Delta\chi^2 = -3.5$). In both these cases, $h_{\rm f}$ and $f_{\rm X}$ are at their maximum values, showing that the fit was searching for the most ionized model available in the grid. Therefore, it is likely that the slight improvement in the fit statistic in these two cases is not significant. The other three observations with $\Delta\chi^2 < 6$ includes another PG 1116+215 spectrum (Obs ID 0554380201), which showed the same behaviour as the other observation just discussed, and two Mrk 590 observations (Obs ID 0601390701 and 0601391001). In the two Mrk 590 observations, $h_{\rm f}$ increased from $\approx$0.4 (as found in the $\lambda = 0.1$ REXCOR grids) to $h_{\rm f} \approx 0.6$–0.7, with $f_{\rm X}$ and τ largely unchanged. However, as the eight other Mrk 590 observations are poorly fit with the high-density REXCOR grid, we conclude that this source is best described using the $\lambda = 0.1$ models.

Table C4. As in Table 2, but now showing the results of the correlation analysis when the REXCOR results for the five observations with negative $\Delta\chi^2$ in Table C1 are used in the analysis (Fig. C1). The significance of the three relationships with λ_{obs} presented in the top half of the table are relatively unaffected with this change. Evidence for the 'v'-shape transition in the τ and h_f relationships with λ_{obs} is lost after switching in the new values, but is recovered after removing the two low λ_{obs} sources that exhibited the largest change in h_f and τ.

Relationship with λ_{obs}	Kendall's τ	p-value
f_X	-0.56 ± 0.06	$2.8^{+31}_{-2.5} \times 10^{-6}$
Γ	0.24 ± 0.06	$0.050^{+0.097}_{-0.037}$
(0.3–10) keV flux ratio	0.56 ± 0.03	$2.8^{+6.6}_{-2.0} \times 10^{-6}$
(0.3–10) keV flux ratio (no RE 1034+396)	0.53 ± 0.03	$1.1^{+2.6}_{-0.8} \times 10^{-5}$
τ and h_f transition λ_{obs} (i.e. $\lambda_{obs,t}$)	Mean p-value	Mean p-value (no Mrk 590 and ESO 198−G24 [Obs ID 0305370101])
0.10	$0.32^{+0.26}_{-0.18}$	$0.16^{+0.33}_{-0.13}$
0.12	0.36 ± 0.14	$0.062^{+0.199}_{-0.049}$
0.15	$0.10^{+0.11}_{-0.06}$	$0.007^{+0.024}_{-0.005}$
0.20	$0.16^{+0.14}_{-0.11}$	$0.12^{+0.08}_{-0.09}$

C2 The coronal height, *h*

For a specific λ (either $\lambda = 0.1$ or 0.01), there are REXCOR grids calculated for two specific heights of the hot, X-ray emitting corona: $h = 5$ or $20\,r_g$ (Xiang et al. 2022). The purpose of these grids is not to make a measurement of h, per se, but to distinguish between a low lamppost (at $h = 5$) and a high lamppost (at $h = 20$), since they lead to different illumination patterns on the accretion disc (e.g. Fukumura & Kazanas 2007; Dauser et al. 2013; Ballantyne 2017).

Table A1 shows the value of h for the REXCOR grid that gives the lowest χ^2. In 13 of the 34 observations (those indicated with a † symbol by the Obs ID) fits with the alternative coronal height have a $\Delta\chi^2 < 6$, which, based on the ΔBIC criterion described above, means that one value of h cannot be preferred over the other. In 9 out of the 13 observations, the warm corona parameters found with the alternative h are consistent with the ones shown in Table A1. For UGC 3973 (Obs ID 040070301) the fit with $h = 20$ gives $\tau = 23.3^{+0.4}_{-3.3}$ (rather than 16.5 ± 0.3), which is still consistent with the observed trends seen in Fig. 3. A value of $h = 5$ when fitting observation (Obs ID 0601390701 of Mrk 509 pushes h_f to 0.76, τ to 16.8, and f_X down to 0.02. When $h = 20$ observation (Obs ID 030248501) of Mrk 279 yields $\tau = 23.8^{+5.6}_{-3.8}$, inconsistent with the value of $\tau = 14^{+4.1}_{-1}$ found when $h = 5$. This new value of τ would pull this observation away from the 'v' shape seen in Fig. 3, reducing its significance. However, all the other observations of Mrk 509 and Mrk 279 give consistent REXCOR parameters when fit with either coronal height. Although we cannot rule out variability intrinsic to the source, since all the observations of these objects have approximately the same λ_{obs}, we expect that the best-fitting values shown in Table A1 remain the most likely results.

Lastly, a coronal height of $h = 5$ decreases both τ and h_f for UGC 3973 (Obs ID 0400070401) to $10.6^{+1.7}_{-0.6p}$ and $0.43^{+0.14}_{-0.11}$, respectively. These values are similar to the ones found in Obs ID 0400070201 of the same source, and are inconsistent with the trends with λ_{obs} seen in Fig. 3. The $h = 20$ and 5 fits both give a reduced $\chi^2 \approx 1$ and so it is difficult to distinguish the two cases. However, this is the only observation where a difference in h may plausibly increase the scatter in the τ–λ_{obs} and h_f–λ_{obs} planes.

C3 The black hole spin, *a*

The REXCOR grids provide different choices for the black hole spin, $a = 0.9$ and 0.99 (Xiang et al. 2022). As with the corona height, the purpose is not to measure a black hole spin with these models, but to test if the data require a maximal spin as compared to a black hole that is simply rapidly spinning. In the REXCOR model, a higher spin not only increases the relativistic blurring and light-bending effects, but it also increases the flux dissipated into the coronae (which are fractions of the dissipation rate $D(r, \lambda)$; Section 2). This effect can be compensated for by reducing f_X, so there is a moderate degeneracy between a and f_X in the REXCOR model (Xiang et al. 2022).

Each AGN in the sample was fit with REXCOR grids using both values of a with the one associated with lowest χ^2 model listed in Table A1. If an AGN has more than one observation, then the value of a found in the first observation was used for subsequent fits. For four AGNs (HE 1029−1401, IRASF 12397+3333, Mrk 509, and NGC 4593; indicated with a '$*$' symbol by the Obs ID in Table A1), assuming the alternative spin when fitting gives a $\Delta\chi^2 < 6$, indicating that either value of a may be considered acceptable. In the cases of HE 1029−1401, IRASF 12397+3333, and NGC 4593, the resulting values of f_X, h_f, Γ, and τ are all consistent irrespective of the choice of a. For Mrk 509, assuming $a = 0.9$ increases f_X by $\approx$0.02 in each of the observations compared to the values listed in Table A1 with the other parameters consistent with the previous results. According to Fig. 4, such a modest change in f_X for the Mrk 509 observations would not alter the observed trend between f_X and λ_{obs}.

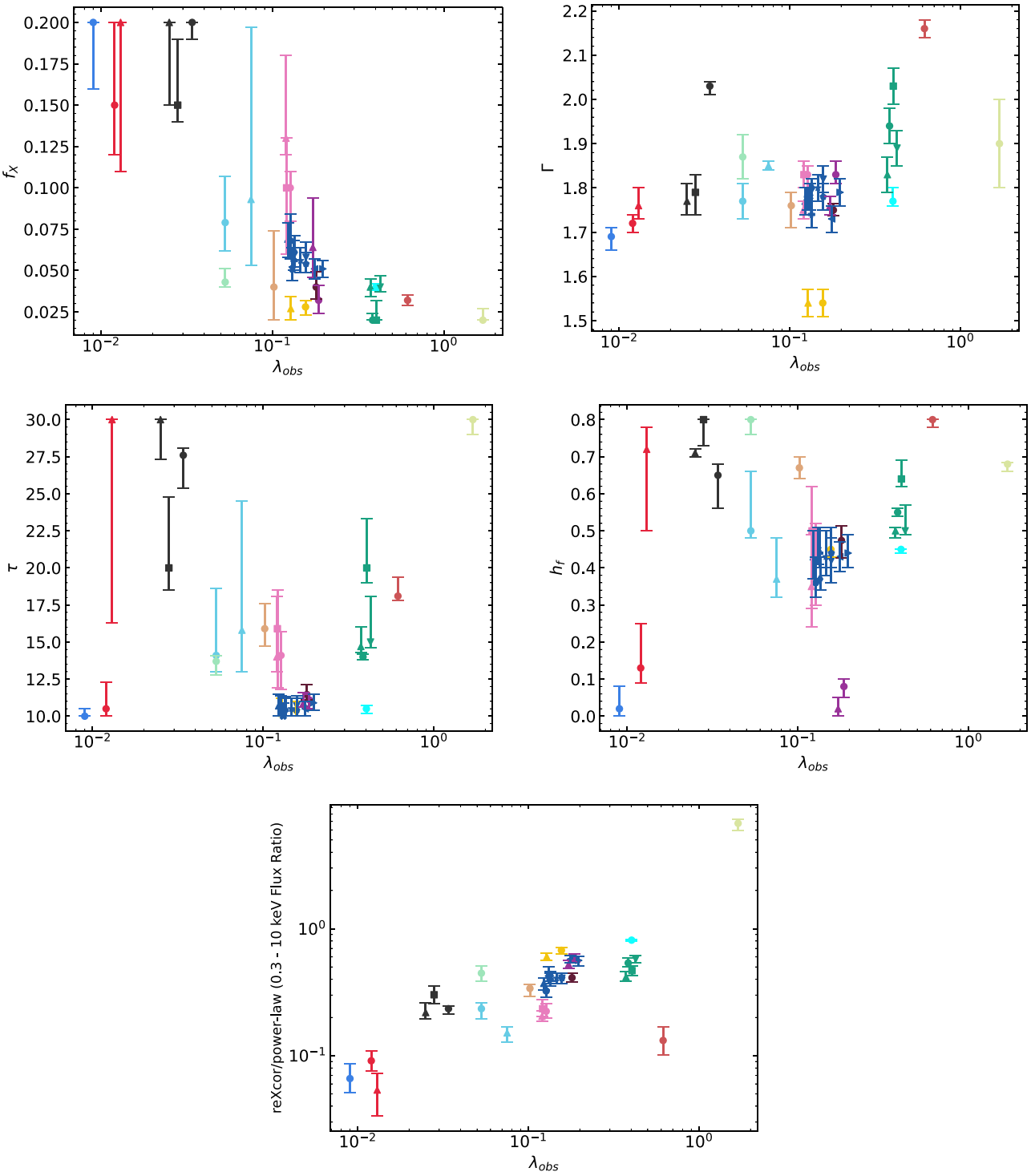

Figure C1. As in Figs 1–4, but now using the results of Table C1 for the five observations that give a negative $\Delta\chi^2$ when using the $\lambda = 0.1$ REXCOR grids. The most significant changes in the REXCOR parameters occur in two of the lowest λ_{obs} in our sample (Mrk 590 and ESO 198−G24 [Obs ID 0305370101]). The resulting statistical analysis is shown in Table C4, which shows that the f_X–λ_{obs}, Γ–λ_{obs}, and the flux ratio–λ_{obs} correlations remain significant, but the 'v'-shaped τ–λ_{obs} and h_f–λ_{obs} relationships are retained only when omitting Mrk 590 and ESO 198−G24 [Obs ID 0305370101].

This paper has been typeset from a TEX/LATEX file prepared by the author.